47

Direct simulation of the turbulent boundary layer along a compression ramp at $M = 3$ and $Re_\theta = 1685$

By NIKOLAUS A. ADAMS

ETH Zürich, Institute of Fluid Dynamics, ETH Zentrum, CH-8092 Zürich, Switzerland

The turbulent boundary layer along a compression ramp with a deflection angle of 18° at a free-stream Mach number of $M = 3$ and a Reynolds number of $Re_\theta = 1685$ with respect to free-stream quantities and mean momentum thickness at inflow is studied by direct numerical simulation. The conservation equations for mass, momentum, and energy are solved in generalized coordinates using a 5th-order hybrid compact-finite-difference-ENO scheme for the spatial discretization of the convective fluxes and 6th-order central compact finite differences for the diffusive fluxes. For time advancement a 3rd-order Runge–Kutta scheme is used. The computational domain is discretized with about 15×10^6 grid points. Turbulent inflow data are provided by a separate zero-pressure-gradient boundary-layer simulation. For statistical analysis, the flow is sampled 600 times over about 385 characteristic timescales δ_0/U_∞, defined by the mean boundary-layer thickness at inflow and the free-stream velocity. Diagnostics show that the numerical representation of the flow field is sufficiently well resolved.

Near the corner, a small area of separated flow develops. The shock motion is limited to less than about 10% of the mean boundary-layer thickness. The shock oscillates slightly around its mean location with a frequency of similar magnitude to the bursting frequency of the incoming boundary layer. Turbulent fluctuations are significantly amplified owing to the shock–boundary-layer interaction. Reynolds-stress maxima are amplified by a factor of about 4. Turbulent normal and shear stresses are amplified differently, resulting in a change of the structure parameter. Compressibility affects the turbulence structure in the interaction area around the corner and during the relaxation after reattachment downstream of the corner. Correlations involving pressure fluctuations are significantly enhanced in these regions. The strong Reynolds analogy which suggests a perfect correlation between velocity and temperature fluctuations is found to be invalid in the interaction area.

1. Introduction

In many cases of practically relevant supersonic flows, shocks and boundary layers are prevalent entities, and at sufficiently high Reynolds number the boundary layers can be transitional or turbulent. A few examples are transonic airfoils, supersonic air intakes, propelling nozzles at non-adapted configuration, and deflected control surfaces of vehicles at transonic or supersonic speed.

Research on shock–boundary-layer interaction has been pioneered by Ackeret, Feldmann & Rott (1946) and Liepmann (1946), who did the first systematic experimental studies on laminar and turbulent boundary layers interacting with normal or

impinging oblique shocks. Since then, research has been based mainly on experimental data, and considerable progress has been achieved in understanding the complex interaction phenomena for laminar and to some extent for turbulent flows.

Adamson & Messiter (1980) give a comprehensive summary of theoretical achievements. The most significant theory is the free interaction theory where viscosity effects are confined to a small near-wall layer. The outer flow is considered to be inviscid and to communicate with the near-wall fluid by a coupling layer, resulting in a triple-deck structure for the interaction system. The main success of the free interaction theory is the derivation of a pressure equation which has been confirmed experimentally for sufficiently high Reynolds numbers (Adamson & Messiter 1980). A theoretical treatment of turbulent flows requires the introduction of another layer into the free-interaction model where Reynolds stresses are dominant. On the basis of this theory Adamson & Messiter (1980) pointed out that the particular choice of a turbulence model does not affect the surface pressure much if there is no separation, which renders surface pressure a rather insensitive measure for quality assessment of turbulence models. More critical is the correct prediction of the skin friction.

Experimental work has continued along the lines given by Ackeret *et al.* (1946) and Liepmann (1946). Canonical configurations were studied at supersonic or transonic flow speeds and at conditions which render the boundary layer laminar or turbulent. Here, we give a brief, and by no means complete, review of more recent experimental work on turbulent supersonic compression ramp flows. Prompted by the requirement of accurate solutions of the Reynolds-averaged Navier–Stokes equations (RANS) by computational fluid dynamics (CFD) for design of supersonic aircraft, experimental databases were established. Settles, Fitzpatrick & Bogdonoff (1979) found that RANS computations with different turbulence models gave poor agreement with experimental skin friction data in cases with large flow separation. Complementary studies by Ardonceau *et al.* (1979) at Mach number $M_\infty = 2.25$ employed laser-Doppler anemometry in comparison with traditional hot-wire sensors. Both studies established that the longitudinal velocity profiles downstream of the interaction area exhibit a two-inflection-point structure. Deflection angles up to 18° were studied and in no case was evidence for a cellular (three-dimensional) large-scale organization in the reattachment region found which could indicate the existence of Görtler vortices in the detached shear layer containing the separation bubble.

Dolling & Murphy (1983) detected a large-scale random shock motion in their ramp data at a free-stream Mach number of $M_\infty = 3$ and a Reynolds number of $Re_{\delta_0} \simeq 10^6$. The observed shock motion spread over a region of 75% to 90% of the mean boundary-layer thickness δ_0. Maximum shock-motion frequencies were found between $f_{sh} = 0.035 f_c$ and $f_{sh} = 0.06 f_c$ where $f_c = U_\infty/\delta_0$ is the characteristic frequency (inverse timescale) of the oncoming boundary layer. These results have been corroborated by Dolling & Or (1985) who found optical evidence for a large-scale shock unsteadiness by high-speed Schlieren photographs. At essentially the same flow parameters as those of Dolling & Murphy (1983), incipient separation was found for a ramp deflection angle of $\beta = 16°$.

Detailed measurements of the fluctuating flow field have been performed by Settles *et al.* (1979) and Smits & Muck (1987) for ramp configurations at similar parameters as Dolling & Or (1985). They confirmed that flow fields were mainly two-dimensional for β up to 16°, where incipient separation was observed. Three-dimensional flow cells in the reattachment area were found for $\beta = 20°$. The fluctuation measurements showed large fluctuation-amplification factors of 5 to 10, along with a change in turbulence structure expressed by the structure parameter a (see §3.5). The large-scale

shock motion which was also observed by Smits & Muck (1987) prompted them to suggest that a 'pumping' mechanism was responsible for turbulence fluctuation amplification by a transfer of shock-motion energy to turbulent kinetic energy. In earlier investigations, Plotkin (1975) found a relationship between shock motion and oncoming boundary-layer turbulence. This issue was taken up by Andreopoulos & Muck (1987) who re-investigated the flow at the same parameters as Smits & Muck (1987). They found that the shock-oscillation spectrum has a significant component at a frequency which corresponds to the incoming boundary-layer bursting frequency. This lead them to the conclusion that shock-oscillation is indeed driven by the oncoming large-scale turbulent fluctuations. This conclusion has sparked a controversial debate. Thomas, Putnam & Chu (1994), for example, objected to the main conclusion of Andreopoulos & Muck (1987) and reported to find no correlation between shock-front oscillation and turbulent bursting events for their transonic normal-shock interaction data. The debate came to a preliminary conclusion by the finding of Erengil & Dolling (1991a) and Erengil & Dolling (1991b) that the shock indeed shows both large-scale and small-scale fluctuations. Both of them are random and seem not to be traceable clearly to turbulence events in the oncoming flow, although there is a correlation between shock motion and pressure fluctuations in the oncoming boundary layer. Also, the separation bubble was found to 'breathe', so that the overall flow structure oscillates with random frequency between a state of small separation and a state of large separation, each of which results in a different shock position and pressure distribution. Spina, Smits & Robinson (1994) state that the shock motion is closely tied to the incoming turbulence field. Also, they give evidence for the validity of the strong Reynolds analogy (SRA), which provides a correlation between temperature and velocity fluctuations based on the similarity of the boundary-layer form of the energy and the momentum equations for a Prandtl number $Pr = 1$, see, e.g. Smits & Dussauge (1996). It is, however, unclear how much experimental evidence for SRA is affected by the data-acquisition technique itself.

Marshall & Dolling (1992) revisit the experimental compression ramp data with the objective of addressing the question of why even sophisticated second-order closure turbulence models fail to predict the correct average wall pressure and skin friction. Concluding from the fact that turbulence models fail dramatically for significant separation only, but show a reasonable performance for attached flows, and from the fact that in most experiments a large-scale shock motion is going along with large-scale separation, Marshall & Dolling (1992) suspected this large-scale low-frequency unsteadiness to be a prime reason for the disagreement between RANS and experiments. Flow-field three-dimensionality – where it is unclear how much this is related to the large-scale unsteadiness – and compressibility effects in the interaction area may be added to this list. Dolling (1998) emphasizes again that the low-frequency expansion–contraction of the separated-flow area is critical in determining the correct time-averaged wall pressure, skin friction, separation location, and downstream velocity profiles. The origin of these fluctuations is, however, still unclear. Intuitively, it seems not to be obvious why some *in situ* instability mechanism should be responsible for a low-frequency forcing, although Smits & Dussauge (1996) suggest an upstream coupling between the reattachment and separation regions across the elliptic separated flow region. It seems more likely, however, that in this case the shock motion and separation-bubble breathing would not be random, but rather lock into a characteristic frequency, contrary to the observations. Some variations in the thermodynamic properties of the oncoming flow (e.g. temperature) may have an effect too, since recorded data by Fernholz *et al.* (1989) and Settles & Dodson

(1991) show some spatial variation in measured reference quantities at the measuring stations.

Theoretical research on turbulence usually follows the strategy of stepwise increasing geometrical and physical complexity. The simplest case is that of isotropic turbulence. This configuration has been subjected to theoretical and numerical study for many years. Linearized theories such as rapid distortion theory (RDT) and linear interaction analysis (LIA) have been re-applied to this problem recently by Lee, Lele & Moin (1993) and Mahesh, Lele & Moin (1993). The results show that turbulent fluctuations are amplified across the shock, where the amplification rate increases with Mach number (Lee *et al.* 1993). Transverse vorticity fluctuations are amplified by a factor of 10 at $M = 3$, for instance. The shock-front distortion depends on the integral lengthscale and the turbulence Mach number. The Taylor microscales consistently decrease across the shock, whereas the dissipation lengthscale increases for Mach numbers less than 2 but decreases for higher Mach numbers. Isotropic turbulence loses isotropy owing to the interaction with the shock and becomes axisymmetric. The degree of compressibility of the incoming turbulence determines the turbulence amplification across the shock, the larger the compressible part of the velocity fluctuations the smaller the turbulence amplification (Hannappel & Friedrich 1995).

The effect of normal-shock strength on isotropic turbulence has been assessed by Mahesh *et al.* (1995) and Lee, Lele & Moin (1997). They show that direct numerical simulation (DNS) and linear interaction analysis (LIA) agree well within reasonable margins concerning the prediction of fluctuation amplification. A consistent decrease of all turbulence lengthscales was observed across the interaction also for strong shocks. Different results were found earlier by Keller & Merzkirch (1990), but the theoretical and DNS results of Lee *et al.* (1997) are conclusive and the experimental results seem to suffer from the data-acquisition technique. For higher Mach numbers (around 2 to 3) the thermodynamic fluctuations become non-isentropic, unlike at lower Mach numbers. The specifics of entropy fluctuations interacting with a normal shock have been investigated by Mahesh, Lele & Moin (1997) who conclude that the temperature–velocity correlation in the oncoming turbulence strongly affects turbulence evolution across the shock. This effect has been explained by the action of bulk compression and baroclinic torque. It was also found that shock-front oscillations invalidate Morkovin's hypothesis (Smits & Dussuage 1996) across the shock.

Physical complexity is increased if allowance is made for (constant) mean shear and shock obliqueness. This case has been studied by Mahesh, Moin & Lele (1996) with the following main findings. The concept of SRA is found not to be valid across the shock. Reynolds stresses decrease for normal shocks, and pressure fluctuations are damped for moderate Mach numbers but amplified for Mach numbers larger than about 3. The amplification of turbulent kinetic energy decreases with increasing shock obliqueness, whereas the Reynolds shear-stress is less damped with increasing shock obliqueness and eventually is amplified for large obliqueness angles. It has also been demonstrated by Mahesh *et al.* (1996) that traditional turbulence models, even second-order closures such as the model by Launder, Reece & Rodi (1975), are unable to predict the correct turbulence structure.

One main objective of experimental, numerical and theoretical studies is the improvement of turbulence models for the solution of the RANS equations. For shock–boundary-layer interaction with significant separation, however, even the explicit modelling of compressibility effects failed to produce an agreement between experiment and RANS computations (e.g. Brankovic & Zeman 1994). Two-equation models

seem to suffer from insufficient upstream influence across the separation area (Wilcox 1994), while the prediction of the pressure plateau in the separated area and of the flow downstream of the separation is fair. Some improvement was achieved by second-order closures, in particular algebraic Reynolds-stress models (Wilcox 1989). Yet, the prediction uncertainty of the separation location is about one boundary-layer thickness and the recovery of the reattached boundary layer is overpredicted. Mean-flow profiles are improved but still differ considerably from experimental measurements in the interaction area.

It is the objective of this paper to gain understanding of the interaction process between a turbulent separated boundary layer and a strong deflection shock. Being the first attempt of a DNS of a flow of such physical complexity, the parameter choice was conservative and was essentially limited by the available computer resources (see Moin & Mahesh (1998) for general remarks on DNS). The Reynolds number is chosen high enough so that the computational domain resides well above the stability limit of the corresponding laminar boundary layer. The precursor turbulent boundary-layer simulation which provides the inflow data gives a momentum thickness Reynolds number of the mean boundary layer at inflow of $Re_\theta = 1685$. The free-stream Mach number has been fixed at $M_\infty = 3$, since this seems to be where most experimental data are available. First, a deflection angle $\beta = 25°$ has been tried in accordance with the experimental data generated by A. Zheltovodov *et al.* at ITAM, RAS Novosibirsk, Russia, at $Re_\theta = 9600$ (partially published by Settles & Dodson 1991). However, the possibility that the expected size of the flow separation conflicted with the restricted streamwise domain size, and that the upstream and downstream effects of the separated flow could interfere with the inflow or outflow boundaries, prompted us to reduce the deflection angle to 18°, where a relatively small separation area was eventually obtained. This is in between the cases of Smits & Muck (1987) at $\beta = 20°$ with a fairly large separation and at $\beta = 16°$ with incipient separation. Since, owing to the significant Reynolds-number differences, comparisons of the computation with the experiments can only be qualitative, we gave preference to the compromise of choosing $\beta = 18°$ in order to obtain a small but more than incipient flow separation.

The DNS limitations are obvious. The small Reynolds number results in a small mean-streamline curvature, and for that reason the shock does not penetrate deeply into the boundary layer since its origin are confluent compression waves emerging from the sonic layer. This is a main difference from high-*Re* experiments, since it also affects the magnitude of the near-wall pressure gradient, which again has an effect on the size of the flow separation. For a given pressure gradient, of course, a smaller *Re* would result in a larger separation. Also, we do not expect to be able to capture streamwise structures with a large spanwise spacing, such as Görtler vortices, owing to the spanwise domain size which we have limited to somewhat more than one mean-boundary-layer thickness. The narrow spanwise domain also poses a considerable restriction on the comparability of the results with experiments, but at this stage it was unavoidable owing to the enormous resources required. In an experimental set-up, a spanwise domain about 10 times larger would be considered sufficient, also to exclude sidewall effects which are not an issue in the computations. Ensemble averaging was limited to 600 samples in time, although about twice as many would be desirable to obtain smooth correlations involving pressure fluctuations or derivatives. We refrained, however, from further continuing this simulation which had already consumed about 6000 CPU hours, and tried to learn as much as possible from the data as they are.
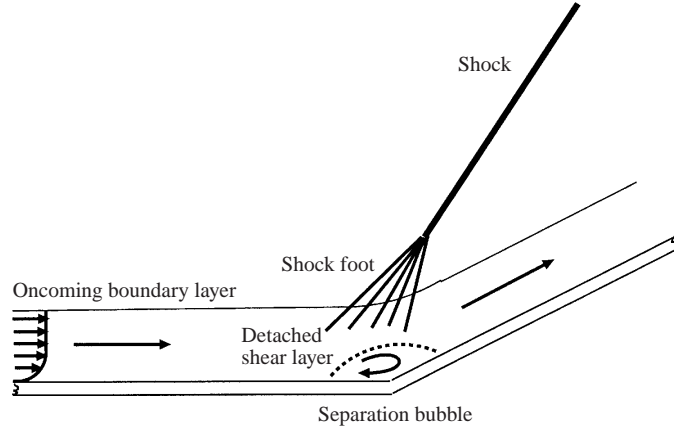
FIGURE 1. Sketch of the compression-ramp configuration.

2. Problem formulation and simulation method

The compression ramp configuration has been chosen in order to increase the physical complexity compared with the homogeneous shear-flow oblique-shock interaction simulations of Mahesh *et al.* (1996). A family of canonical configurations for shock–turbulence interaction has been devised by Green (1970). Among these are the compression ramp, the oblique shock reflection and the case of a normal shock interacting with a boundary layer. The compression ramp, see figure 1, is a standard test case for turbulence modelling, and a wealth of experimental data is available (although at significantly higher Reynolds number than presently affordable by DNS). It also has some technical advantages over the other cases. Since the shock is generated at the boundary-layer edge, close to the corner, and emanates outward through the outflow part of the computational domain, the need to impose an impinging shock accurately at the far-field boundary is avoided. Also, the required computational domain size is reduced in comparison with the case of an oblique impinging shock. These advantages seem to justify the additional computational cost required for a generalized-coordinate formulation in the case of a compression ramp.

We chose a ramp deflection angle of $\beta = 18°$ as a compromise between being able to capture desired large-scale flow features, such as mean-flow separation, and the limited computational resources. For $\beta = 18°$, we expect a small flow separation only, with the benefit that some effects of separation can be studied, without requiring excessive computational domain sizes. In the case of a larger deflection angle, a significant increase of the streamwise (and possibly spanwise) extent of the computational domain would be necessary to resolve the separation area properly and to decouple it sufficiently from inflow and outflow boundaries. Nevertheless, the required computational resources were considerable: the flow field was discretized by about 15×10^6 grid points; the computation required about 750 hours of 8 vector CPUs of a NEC SX-4 running in parallel; the main memory requirement was about 3.5 GBytes and about 400 GBytes of data have been stored in mass storage for postprocessing.

2.1. *Mathematical model*

For convenience, a tensor notation (with summation convention) is used in the following, where the subscripts 1, 2 and 3 correspond to the streamwise, spanwise, and wall-normal coordinate, respectively. We write the fundamental equations in the
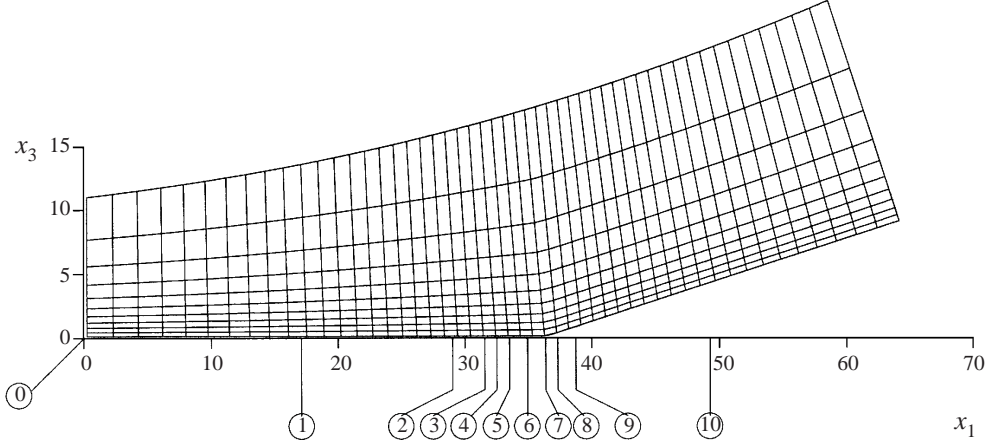
FIGURE 2. Computational mesh (each 20th line); numbers in circles indicate stations where profiles are shown in § 3.

Cartesian (x_1, x_2, x_3) physical space, using a transformation to computational space (ξ_1, ξ_2, ξ_3) which is detailed in Adams (1998). Considering essentially two-dimensional configurations only, we limit the coordinate generalization to the (x_1, x_3)-plane, and x_2 is mapped onto ξ_2 linearly. Figure 2 shows a side-view of the computational domain, where only each twentieth mesh line is displayed.

In the following, dimensional quantities are marked by an asterisk. As a reference length, we use the displacement thickness δ_1^* of the mean boundary layer at inflow. The integration domain has the extents $L_1^* = 63.8\,\delta_1^*$ in the streamwise and $L_2^* = 2.9\,\delta_1^*$ in the spanwise direction, and is truncated at L_3^* varying between $10.9\,\delta_1^*$ and $21.4\,\delta_1^*$ in the wall-normal direction. We assume the solution to be L_2-periodic in x_2.

A perfect gas with a specific-heat ratio of $\gamma = 1.4$ is assumed and the viscosity is calculated according to Sutherland's law with a reference temperature T_∞^*. The non-dimensionalization is carried out by

$$u_i = u_i^* / U_\infty^*, \quad \rho = \rho^* / \rho_\infty^*, \quad T = T^* / T_\infty^*, \quad p = p^* / (\rho_\infty^* U_\infty^{*\,2}), \quad E = E^* / (\rho_\infty^* U_\infty^{*\,2}).$$

Here, the u_i terms denote the Cartesian velocity components, ρ the density, p the pressure and $E = p/(\gamma - 1) + \rho u_i u_i / 2$ the total energy. The time t is non-dimensionalized by δ_1^* / U_∞^*.

Given a Reynolds number $Re = U_\infty^* \rho_\infty^* \delta_1^* / \mu_\infty^*$ and a Mach number $M = U_\infty^* / a_\infty^*$, we can write the compressible Navier–Stokes equations in curvilinear coordinates as

$$\frac{\partial}{\partial t}\frac{U}{J} + \frac{\partial}{\partial \xi_1}\frac{F_E}{J} + \frac{\partial}{\partial \xi_2}\frac{G_E}{J} + \frac{\partial}{\partial \xi_3}\frac{H_E}{J} = \frac{\partial}{\partial \xi_1}\frac{F_S}{J} + \frac{\partial}{\partial \xi_2}\frac{G_S}{J} + \frac{\partial}{\partial \xi_3}\frac{H_S}{J}, \tag{2.1}$$

where the conservative variables are $U = \{\rho,\ \rho u_1,\ \rho u_2,\ \rho u_3,\ E\}$, and J is the Jacobian of the mapping $(x_1, x_2, x_3) \leftrightarrow (\xi_1, \xi_2, \xi_3)$. F_E, G_E, H_E are the convective fluxes and F_S, G_S, H_S are the diffusive fluxes in the respective coordinate directions. For the detailed flux definitions, refer to Adams (1998).

Boundary conditions are as follows. At the inflow, we prescribe all variables in time, using data from a separate spatial boundary layer DNS, see § 3.1. At the outflow, a sponge-layer technique is used, which is detailed in Adams (1998). At the upper truncation plane, free-stream conditions are imposed. The wall is assumed to be isothermal, and no-slip conditions are imposed on the velocity. The isothermal-wall

condition appears to be appropriate for a turbulent flow since the wall-temperature response to temperature changes in the ambient fluid is rather slow owing to the comparably large heat capacity of the immersed body. Experimental conditions are closer to adiabatic for the statistical mean. Evidence, however, that isothermal-wall boundary conditions are an appropriate approximation for the rather complex heat-exchange mechanisms between the turbulent flow and the immersed body is given by the data of Zheltovodov (Settles & Dodson 1991), where the mean wall temperature varies only by about 10% to 20% across the compression region. Further details on the mathematical model and the boundary-condition implementation can be found in Adams (1998).

2.2. *Numerical method*

In this section we briefly summarize the numerical approach. For details, we refer to the given references. For the spatial discretization of the convective terms in equation (2.1) a hybrid compact-ENO finite-difference scheme is used (Adams & Shariff 1996). In smooth regions, this scheme is similar to the Padé schemes of Lele (1992*a*), it is, however, upwind biased owing to asymmetric coefficients of the centred stencil. The scheme is consistently of 5th order in smooth regions (including boundaries), has a 5-point stencil and good dispersion preserving properties. Aliasing errors are diminished by a controlled amount of artificial dissipation of 6th order at non-resolved wavenumbers. Around discontinuities the scheme is coupled with an essentially non-oscillatory (ENO) scheme of 4th order (Shu & Osher 1989), which has good shock-capturing properties. The diffusion terms are discretized with a 6th-order compact finite-difference scheme of Lele (1992*a*). The spatially discretized equations are advanced in time with an explicit low-storage 3rd-order Runge–Kutta scheme (Williamson 1980). A comprehensive description of the numerical algorithm, also addressing issues of the efficient implementation of the coupling algorithm, and validation results can be found in Adams & Shariff (1996) and Adams (1998).

As mentioned in the previous section, Dirichlet-type boundary conditions are imposed at the upper truncation plane. For discretization schemes without numerical diffusion, non-reflecting boundary conditions are often implemented instead, in order to diminish wave reflections at the boundary. In our case, the mesh coarsening towards the boundary lets the numerical diffusion of the discretization scheme act as a filter which removes spurious wave-reflections from the boundary.

3. Simulation results

The simulation parameters are summarized in table 1. Ninety-seven of the total $N_3 + 1 = 181$ grid points reside within the mean boundary layer at the inflow, which gives an average spacing over the height of the boundary layer at the inflow of $\Delta_{x_3}^+ \simeq 2.3$. The first gridpoint off the wall is at $\Delta_{x_3}^+ = 1.4$. The fact that the numerical scheme is consistently of high order up to the boundaries relaxes the near-wall resolution requirements compared with lower-order schemes. Sufficient wall normal resolution is assessed from the fact that the law of the wall is correctly represented, figure 7(*a*), for which it is necessary that near-wall gradients are accurately computed. For the statistical data presented in the following, 600 samples were taken over a time interval of about $t_s = 915$, which corresponds to about 10 flow-through times. In the following, we present profile data along certain computational grid lines $\xi_1 = $ const. For the location of these lines, we refer to figure 2 which shows a side view of the

Parameter	Value	Comment
M_∞	3	
Re_{δ_1}	8977	
Re_θ	1685	using v_∞
Re_{δ_2}	732	using v_w
δ_0	2.38	at inflow
θ	0.19	at inflow
T_∞^*	115 K	
T_W	$2.522 T_\infty^*$	
S^*	110.4 K	
β	18°	
L_{x_1}	63.80	
L_{x_2}	2.90	
L_{x_3}	10.87	at inflow
N_1	1000	
N_2	80	
N_3	180	
$\Delta_{x_1}^+$	6	at inflow
$\Delta_{x_2}^+$	3.3	at inflow
$\Delta_{x_3}^{+\,(1)}$	1.4	at inflow

TABLE 1. Simulation parameters.

computational domain. The relevant positions are marked with numbers which we refer to in the following.

3.1. *Inflow data*

Inflow data for the compression ramp simulation were generated by a separate DNS of a spatially evolving zero-pressure-gradient turbulent flat plate boundary layer. This simulation itself required inflow data which were taken from a temporal DNS. In this temporal DNS, a turbulent flow was obtained by employing a bypass transition mechanism where linearly stable oblique modes are initialized with a finite amplitude leading to transient growth from a background-noise seed and eventually to laminar–turbulent transition, see e.g. Haniff, Schmid & Henningson (1996). This procedure is more efficient than starting the temporal DNS from non-physical initial conditions. To reduce computational cost, the spatial boundary layer DNS was run only for $t_{si} = 70\delta_0/U_\infty$. About 18 mean boundary-layer thicknesses downstream of the inflow the instantaneous flow of the spatial boundary layer DNS was sampled and all dependent variables in a cross-flow plane (x_2, x_3) were stored. A thousand such samples were taken. Since the inflow data were used for larger integration times than t_{si}, the data were made periodic in time artificially by linearly blending the time-interval ends. The inflow data for an arbitrary time t are then obtained by interpolating the data at time $\mathrm{mod}(t, t_{si})$ with a third-order polynomial interpolation. By this construction, we avoid an artificial forcing of a frequency in the range of the characteristic frequency of the boundary layer or smaller, since in a preliminary computation it was found that this affects the shock and separation dynamics (Adams 1997). The time span t_{si} is large enough to ensure that the inflow data are sufficiently decorrelated before they repeat. The computational cost for generating the inflow data from a precursor boundary-layer simulation was roughly 10% of that for the compression ramp simulation. A larger time sequence t_{si} would certainly have improved statistical averages, but we found the increase of computational cost impractical. The maximum amplitude at
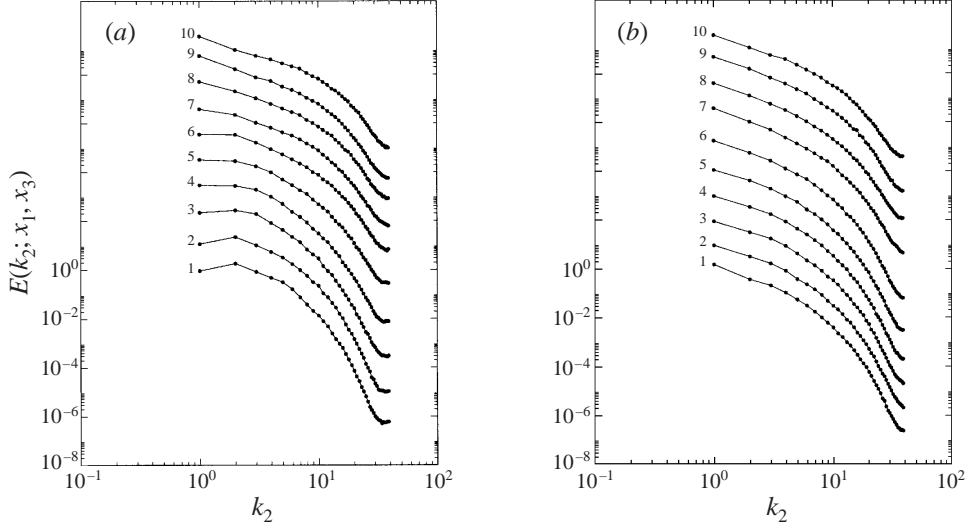
FIGURE 3. $E(k_2; x_1, x_3)$ at downstream positions 1–10 (bottom-up), and (a) $x_3^+ = 5$, (b) $x_3^+ = 97$ with respect to inflow; spectra are shifted by a factor of 10 for clarity.

inflow of the streamwise velocity fluctuation u_1'' is about 7%, and of the temperature fluctuation T'' about 15%.

3.2. *Assessment of resolution*

The enormous computational effort makes grid-independence studies impractical for DNS. After thorough design and validation of the numerical method the flow parameters for the actual simulation were chosen in order to make best possible use of the available computational resources. By trial parameter variations the parameter set given in table 1 was found suitable. An assessment of the spatial resolution is facilitated by periodicity in the x_2-direction. A sufficiently accurate spatial discretization is indicated by the fact that suitable norms of the solution decay sufficiently fast in Fourier-transform space. A Fourier expansion of the solution is possible in the periodic x_2-direction. Under-resolution in the directions x_1 and x_3 would reflect in the k_2 spectra owing to aliasing across the wavenumber-vector components. We choose as norm the spectral kinetic energy which we compute from the velocity components

$$u_i(x_1, x_2, x_3) = \sum_{k_2 = -N_2/2}^{N_2/2 - 1} \hat{u}_i(x_1, x_3)\, e^{i2\pi k_2 x_2/L_2} \tag{3.1}$$

as

$$E(k_2; x_1, x_3) = \hat{u}_i(k_2; x_1, x_3)\, \hat{u}_i^*(k_2; x_1, x_3), \tag{3.2}$$

where the asterisk indicates the complex conjugate (we use the summation convention for equal indices).

Figure 3 shows the energy spectra at the 10 downstream stations defined by the intersection of lines $\xi_1 = \text{const}$ and $\xi_3 = \text{const}$, as indicated in figure 2. The longitudinal coordinate lines $\xi_3 = \text{const}$ go through the points $(x_1 = 0, x_3^+ = 5)$ and $(x_1 = 0, x_3^+ = 97)$, respectively. In all cases, we find that the spectra decay by 5 to 6 orders of magnitude, without a significant pile-up close to the Nyquist wave number, which indicates that all relevant scales are well resolved.
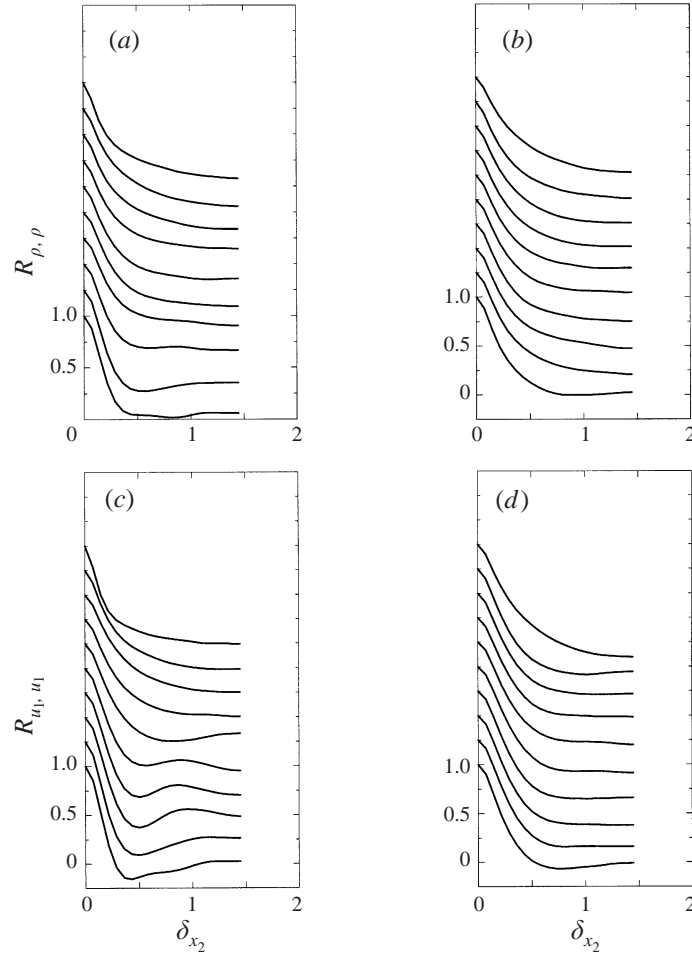
FIGURE 4. Two-point correlations for downstream stations 1–10 (bottom-up), (*a*) $R_{\rho,\rho}$ at $x_3^+ = 5$, (*b*) $R_{\rho,\rho}$ at $x_3^+ = 97$, (*c*) R_{u_1,u_1} at $x_3^+ = 5$ and (*d*) R_{u_1,u_1} at $x_3^+ = 97$; curves shifted by 0.25 for clarity.

Another issue is the sufficiency of the domain size in the spanwise direction, where a periodic boundary condition is enforced. For a periodic boundary condition to be reasonably accurate the two-point correlations of the solution are required to be close to zero at a distance of half the domain size. In figure 4, we show the two-point correlations for ρ and u_1 at the downstream stations 1–10 and the wall normal positions $x_3^+ = 5$ and $x_3^+ = 97$ corresponding to the positions where the energy spectra are shown in figure 3. Table 2 gives the values of all primitive-variable two-point correlations at $\delta_{x_2} = 1.45 = L_2/2$. The magnitude of $R_{\rho\rho}$ (density correlations) close to the wall decays to values between 6% and 7%. The velocity correlations assume values up to 10% to 15%, which can be an indication of a tendency to build a coherent crossflow structure. This is also indicated by the spectral kinetic energy which is maximum for the modes $k_2 = \pm 1$, figure 3. The pressure correlation R_{pp} assumes significant values at $\delta_x = L_2/2$ near the ramp corner. It should be noted that crossflow structures with a spanwise wavelength larger than the spanwise domain size cannot be represented in the simulation, see also § 3.4. The limited computer memory made it, however, impossible at this stage to further increase the spanwise
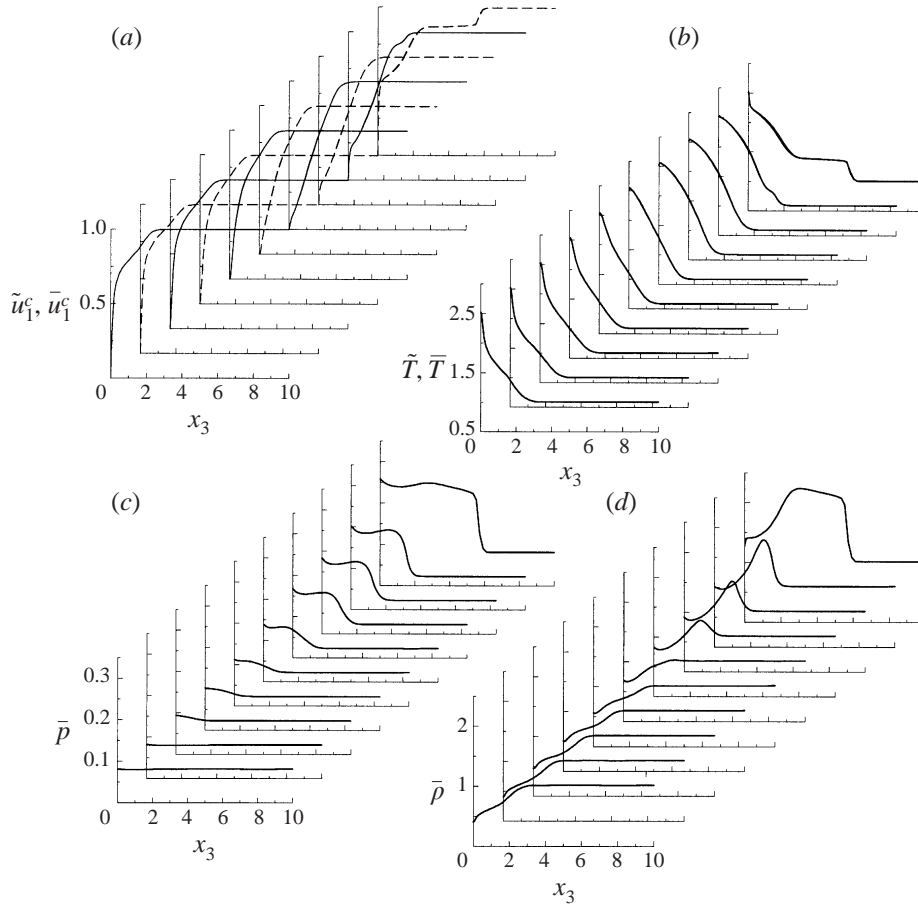
FIGURE 5. (*a*) Alternating —— and – – – – for $\tilde{u}_1^c$ (thick lines) and for $\bar{u}_1^c$ (thin lines); (*b*) ——, $\tilde{T}$ (thick lines) and ——, $\bar{T}$ (thin lines); (*c*) $\bar{p}$, and (*d*) $\bar{\rho}$ at downstream stations 1–10 according to figure 2. Note that in (*a*) and (*b*) although two lines (thick and thin) are shown at each station, they mostly overlap and are indistinguishable.

domain size. The turbulence structure of the flow is probably less affected by the small spanwise-domain size which is larger than the minimal flow unit established by Jimenez & Moin (1991).

3.3. *Mean flow*

The mean flow profiles are plotted along computational mesh lines $\xi_1 = const$ for the downstream stations 1 to 10, figure 5. The velocity vectors are shown in their contravariant representation. Velocity and temperature are Favre averaged, and for comparison the corresponding Reynolds averages are shown also. The Favre or mass averages are computed from $\tilde{f} = \overline{\rho f}/\bar{\rho}$, where the overbar denotes the Reynolds or ensemble average. Where applicable, we make use of the spanwise homogeneity, and averages were obtained by computing the arithmetic mean over all time samples and over all grid points in x_2. Favre averaging not only simplifies the averaged compressible Navier–Stokes equations but is also the natural way of extracting average primitive variables from averaged conservative variables which are the primary variables for a compressible flow. Naturally, from the equation of state then the Favre-averaged temperature $\tilde{T}$ appears as the consistent supplement

Station	$R_{\rho\rho}$ $x_3^+ = 5$	$R_{\rho\rho}$ $x_3^+ = 97$	$R_{u_1 u_1}$ $x_3^+ = 5$	$R_{u_1 u_1}$ $x_3^+ = 97$	$R_{u_2 u_2}$ $x_3^+ = 5$	$R_{u_2 u_2}$ $x_3^+ = 97$	$R_{u_3 u_3}$ $x_3^+ = 5$	$R_{u_3 u_3}$ $x_3^+ = 97$	R_{pp} $x_3^+ = 5$	R_{pp} $x_3^+ = 97$
1	0.06	0.02	0.02	−0.01	−0.006	−0.05	−0.01	−0.02	0.11	0.12
2	0.10	−0.04	0.02	−0.09	−0.04	−0.03	−0.01	0.02	0.16	0.14
3	0.17	−0.03	−0.01	−0.12	−0.09	−0.04	−0.001	0.01	0.23	0.19
4	0.16	0.01	−0.05	−0.09	−0.08	−0.06	−0.01	0.009	0.11	0.32
5	0.09	0.05	−0.05	−0.09	−0.08	−0.03	−0.02	0.04	0.08	0.41
6	0.11	0.05	0.08	−0.05	−0.08	−0.06	−0.005	0.03	0.09	0.23
7	0.15	0.02	0.005	−0.02	−0.05	−0.15	0.02	−0.02	0.16	0.18
8	0.09	0.01	0.003	−0.03	−0.08	−0.10	0.02	−0.02	0.12	0.15
9	0.10	0.01	−0.01	−0.05	−0.08	−0.09	0.03	−0.02	0.12	0.15
10	0.11	0.03	−0.05	−0.15	−0.07	−0.08	0.01	0.05	0.13	0.19

TABLE 2. Values of the two-point correlation functions of the primitive variables at $\delta_{x_2} = L_2/2$, at stations 1–10 and following mesh-planes starting at $(x_1 = 0,\ x_3^+ = 5)$ and $(x_1 = 0,\ x_3^+ = 97)$, respectively.

Profile	$x_{3\,sonic}$	$x_{3\,sonic}^+$
1	0.15	10
2	0.18	11
3	0.25	8
4	0.35	—
5	0.48	—
6	0.88	—
7	1.28	—
8	1.29	37
9	1.28	50
10	0.25	14

TABLE 3. Mean sonic layer position.

to the Favre-averaged set of primitive variables $\bar{\rho}, \tilde{u}_i, \bar{p}$. In the following, we refer to the contravariant velocities $u_1^c = (u_1 \partial \xi_1/\partial x_1 + u_3 \partial \xi_1/\partial x_3)/\sqrt{(\partial \xi_1/\partial x_1)^2 + (\partial \xi_1/\partial x_3)^2}$, $u_2^c = u_2$, and $u_3^c = (u_1 \partial \xi_3/\partial x_1 + u_3 \partial \xi_3/\partial x_3)/\sqrt{(\partial \xi_3/\partial x_1)^2 + (\partial \xi_3/\partial x_3)^2}$. The difference between contravariant components and longitudinal components, where the velocity vector is rotated into a Cartesian system aligned with the wall, is small. A contravariant projection allows, however, for a consistent definition across the integration domain, whereas the longitudinal projection is ambiguous near the corner.

From the velocity profiles we see the typical deformation due to an adverse pressure gradient, figure 5(*a*), and at the last station, 10, the profile shows a wake-like shape. Differences between $\bar{u}_1$ and $\tilde{u}_1$ are very small throughout the domain (the same holds for the other velocity components). The differences between Reynolds and Favre averages for the temperature are small but visible, within and after the interaction region, figure 5(*b*). When $\tilde{T}$ and $\bar{T}$ differ but $\tilde{u}$ and $\bar{u}$ are almost identical, it can be concluded that density fluctuations assume a significant magnitude but are uncorrelated with the velocity fluctuations. This can be observed from the identity $\tilde{f} - \bar{f} = \overline{\rho' f'}/\bar{\rho}$ for some variable f. In other words, density does not behave as a passive flow property.

Owing to the low Reynolds number, the mean boundary layer does not exhibit any significant thinning downstream of the interaction. The mean boundary-layer
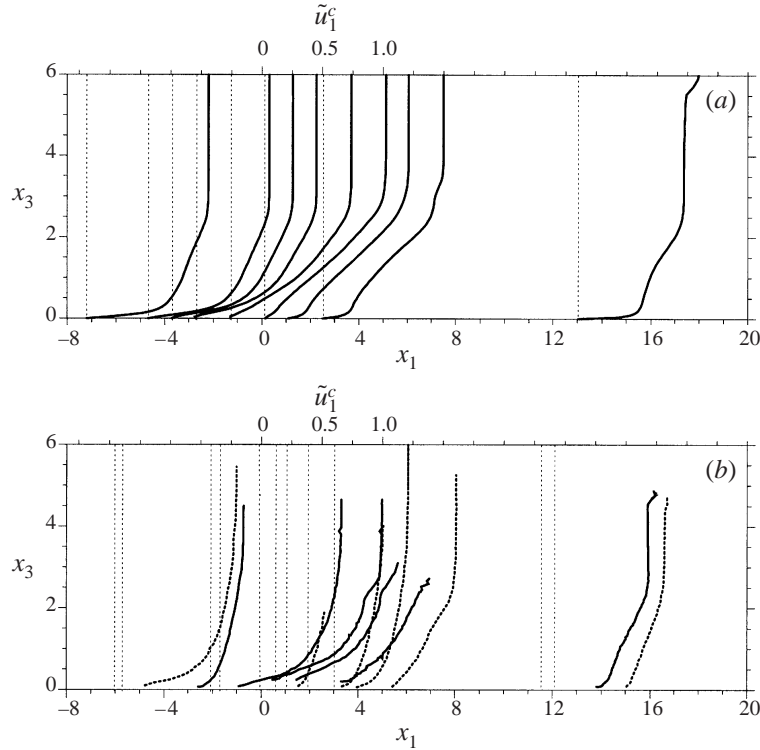
$\tilde{u}_1^c$

FIGURE 6. Downstream evolution of mean velocity profiles $\tilde{u}_1^c$: (*a*) for the simulation, (*b*) for ExpB ($\cdots\cdots$) and ExpC (——) of Smits & Muck (1987), data from Settles & Dodson (1991); thin dotted vertical lines are reference lines indicating the downstream position x_1 from the ramp corner (lower horizontal axis); the magnitude of $\tilde{u}_1^c$ (upper horizontal axis) is measured from the respective reference lines; for the experiments $\tilde{u}_1^c$ is given along wall-normal coordinate lines.

thickness at station 10 is about 95% of the boundary-layer thickness at station 1. This differs from what is observed for high-Reynolds-number experiments (Smits & Muck 1987) but agrees with the lower Reynolds-number experiments of Zheltovodov *et al.* (Settles & Dodson 1991). In figure 6(*a*), the downstream evolution of the $\tilde{u}_1^c$ profiles is shown at stations 2 to 10. For reference, experimental profiles for the cases with $\beta = 16°$ and with $\beta = 20°$ of Smits & Muck (1987), hereinafter referred to as ExpB and ExpC, are shown in figure 6(*b*).

The adverse pressure gradient is felt first near the wall, where upstream propagation is facilitated owing to the elliptic character of the flow beneath the sonic line, figure 5(*c*). For reference, the position of the mean sonic layer is given in table 3, including the wall-distance in wall-units where applicable. Since the wall temperature is kept constant at the pre-shock value across the domain, the density near the wall increases according to the pressure rise behind the shock, figure 5(*c*). Across the shock, the density increases according to the jump relations (the compression ratio is 3.4). The higher-density fluid is transported towards the wall by turbulent diffusion until it reaches the boundary-layer edge, where it mixes with lower density near-wall fluid. This process results in a wedge-like high-density region between the shock and the wall. Pressure adjusts faster across the boundary layer than density and temperature. The post-shock pressure shows only small variation across the boundary layer. The mean shock location is clearly visible in the profiles at station 10 (note that the shock is smeared owing to averaging). We also note that the mean-temperature profiles are

close to adiabatic ones at stations 1 to 9. At station 10, where hot fluid reaches the wall, a significant mean-temperature gradient appears at the wall, which would not be the case for adiabatic-wall boundary conditions. The effect of a wall heat flux, however, can be expected to be confined to a small internal layer close to the wall (Debiéve *et al.* 1997; Maeder, Adams & Kleiser 2000).

Scaled in local wall units, contravariant velocity profiles at relevant stations (with positive C_f) are shown in figure 7. At position 1, we find that the van Driest transformed mean velocity (e.g. Smits & Dussauge 1996) $\bar{u}_{1_{VD}}$ agrees with the law of the wall $\bar{u}^+_{1_{VD}} = 2.5 \ln(z^+) + 5.5$, although the logarithmic region collapses to an inflection point owing to the low Reynolds number. The non-transformed velocity $\bar{u}^+$ at station 1 undershoots the law of the wall. The downstream profile-evolution follows a similar trend as was found by Smits & Muck (1987) for their experimental data. The entire profile overshoots the wall-law close to separation, station 2, as is typical for an adverse-pressure-gradient boundary layer (Na & Moin 1998). This trend continues through the last profile at station 3 before mean-flow separation. Within the region of mean-flow separation wall-scaling has no meaning and profiles are not shown. After mean-flow reattachment at station 9 the boundary layer has recovered in a similar fashion to the downstream profiles of Smits & Muck (1987). What is often called a 'dip' below the wall-law can be seen. Also visible is a region of almost constant slope. The profiles after reattachment are similar to those observed by Na & Moin (1998) for a flat-plate boundary layer with separation. All profiles show an indication of a logarithmic region. By matching the profiles with a wall-law, von Kármán constants of $\kappa = 0.30$ and $\kappa = 1.8$ are obtained, where the integration constant of the wall-law changes to 2.5 and 2 for stations 2 and 9, respectively. Note that for post-processing, the mesh has been coarsened by a factor of 2 in each direction. Accordingly, the first mesh point as shown is in fact the second mesh point in the computation.

The skin friction coefficient $C_f = 2\,\bar{\sigma}^{\perp}_{13}$, where $\sigma^{\perp}_{13}$ denotes the shear component for the viscous stress in a coordinate system following the wall, exhibits a sudden drop at mean-flow separation followed by a steep increase at reattachment, figure 8(a). The extent of the mean-flow separated area can be estimated from the part where C_f is negative ($C_f = 0$ is indicated by a thin line). For reference, we show the experimental data for the cases ExpB and ExpC. Re_θ for ExpB and ExpC is about 50 times larger than for the computation; hence, the overall much lower skin friction compared with the computation. Since the experimental data do not provide negative values of skin friction, the size of the mean-flow separation for case ExpC is estimated to be about three displacement thicknesses of the incoming boundary layer. Note that in the computation, the corner is approximated smoothly by a small radius which is resolved numerically (see Adams 1998). Reattachment takes place shortly behind the corner. Also shown is the surface pressure p_{surf} and its derivative $p'_{surf} = \mathrm{d}p_{surf}/\mathrm{d}x$, figure 8($b$). The derivative p'_{surf} shows a sequence of three inflection points of p_{surf} (maximum-minimum-maximum of p'_{surf}) in the mean-flow separated area (first and last are indicated by arrows). The existence of a sequence of three inflection points is one criterion of mean-flow separation, as given by Green (1970). For reference, also the experimental surface-pressure distributions of ExpB and ExpC are given. A pressure plateau as predicted by the free-interaction equations (Adamson & Messiter 1980), which is clearly present in the high-Reynolds-number experimental data ExpC, is not visible at the low Reynolds number of the computation. The surface-pressure distributions reach the levels predicted by inviscid theory which are indicated by dotted lines in figure 8(b). The upstream influence length L_{up} can be estimated from a tangent criterion (Katzer 1989). For the computation, $L_{up} = 2.3\,\delta_0$
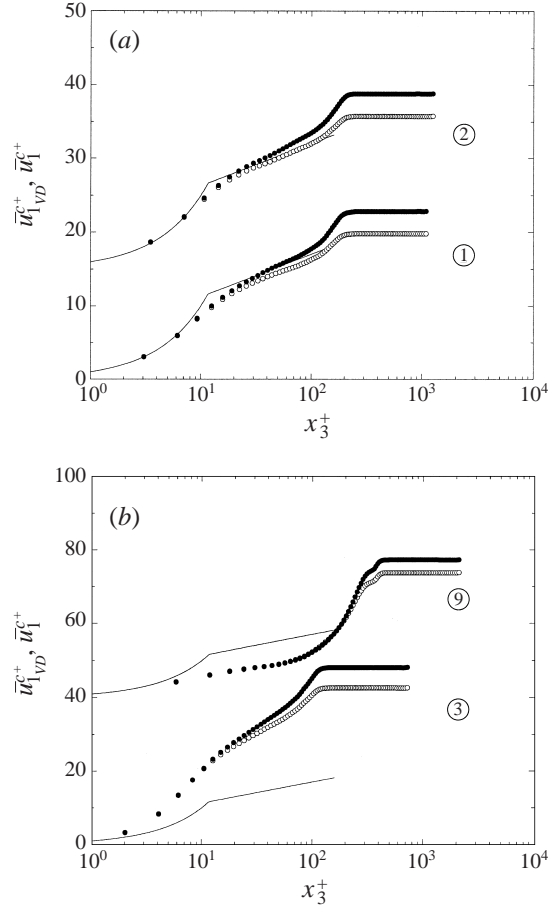
FIGURE 7. Contravariant-velocity profiles scaled in wall units; (*a*) at stations 1 and 2, bottom-up; (*b*) at stations 3 and 9 bottom-up; $\circ$, $\bar{u}_1^{c+}$; $\bullet$, $\bar{u}_{1_{VD}}^{c+}$; ———, law of the wall x_3^+ and $(2.5\ln(x_3^+) + 5.5)$; for clarity staggered by 15 and 40, respectively.

upstream of the corner is obtained, which compares well with the experimental data.

3.4. *Shock-wave structure and separation*

For an overview of the instantaneous flow behaviour, we first consider a computed Schlieren visualization of the instantaneous density-gradient magnitude averaged over the spanwise coordinate x_2 in figure 9(*a*). This corresponds roughly to a spark shadowgraph of the flow, compare, for example, with figure 3*a* of Dolling & Murphy (1983). Evidently, turbulence lengthscales decrease across the interaction region. This agrees with an observed decrease of the Taylor microscale λ, equation (3.5), from $\lambda = 0.22$ at station 1 to $\lambda = 0.16$ at station 10 for a fixed distance above the wall of $x_3 = 1.96$. Note that the values for λ in table 4 are along a meshline which detaches from the wall downstream, i.e. the distance from the wall at station 10 is larger than that at station 1. The shock foot is the origin of a high density-gradient interface at the boundary-layer edge, which extends downstream. Owing to the low Reynolds number, the mean-streamline curvature is small and the confluence point of compression waves, which radiate from the sonic layer outwards to build the shock,
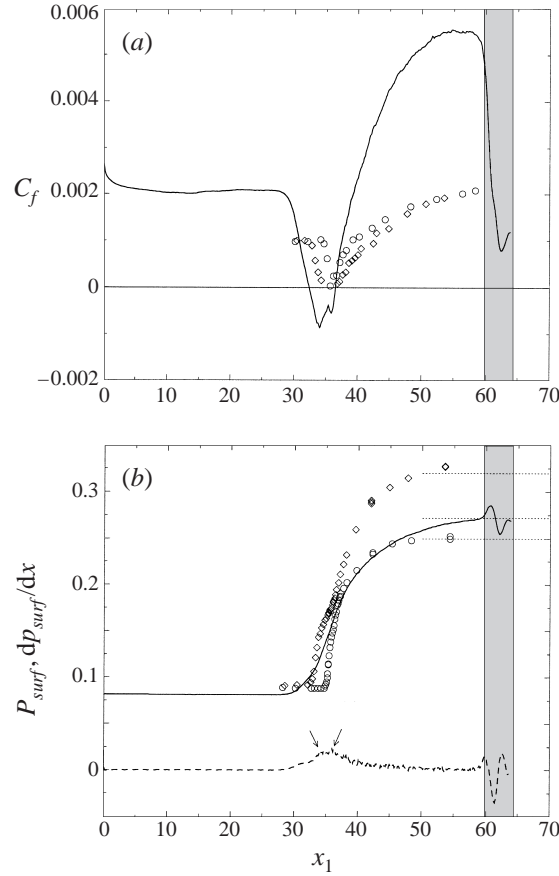
FIGURE 8. (*a*) ——, C_f and (*b*) ——, p_{surf}, also shown is - - -, $\mathrm{d}p_{surf}/\mathrm{d}x$; grey shaded area indicates the sponge region, arrows indicate first and last inflection point of p_{surf}; O, experimental results ExpB; ◇, experimental results ExpC.

is located closer towards the boundary-layer edge than is observed in high-Reynolds-number experiments, see Smits & Muck (1987) or Ardonceau *et al.* (1979). For comparison, we also show the corresponding computed Schlieren visualization for the stationary flow, averaged over 100 samples, in figure 9(*b*). The area of unsteady shock-motion is apparent from a comparison of the instantaneous shock location in figure 9(*a*) with its mean location in figure 9(*b*). For a comparison with the visualized simulation data, an experimental Schlieren visualization of a $M_\infty = 2.9$ boundary layer along a $\beta = 25°$ compression ramp at $Re_\theta = 9600$ (kindly provided by A. Zheltovodov, ITAM, Novosibirsk) is shown in figure 10, where the compression waves emanating from the boundary-layer edge are clearly visible.

A three-dimensional visualization illustrates the instantaneous shape of the shock front, figure 11. The shock is visualized by a surface of constant negative velocity divergence $\partial_{x_i} u_i = -0.4$. The shock forms in the outer part of the boundary layer and fringes towards the wall. This fringing has also been called 'spanwise shock wrinkling' as it appears in experimental visualizations (Smits & Muck 1987). It is caused by the unsteadiness of the sonic layer and the outward radiating compression waves. The colour coding in figure 11 corresponds to local density, which is shown at the wall, the rear boundary of the computational domain, and in four crossflow planes. The
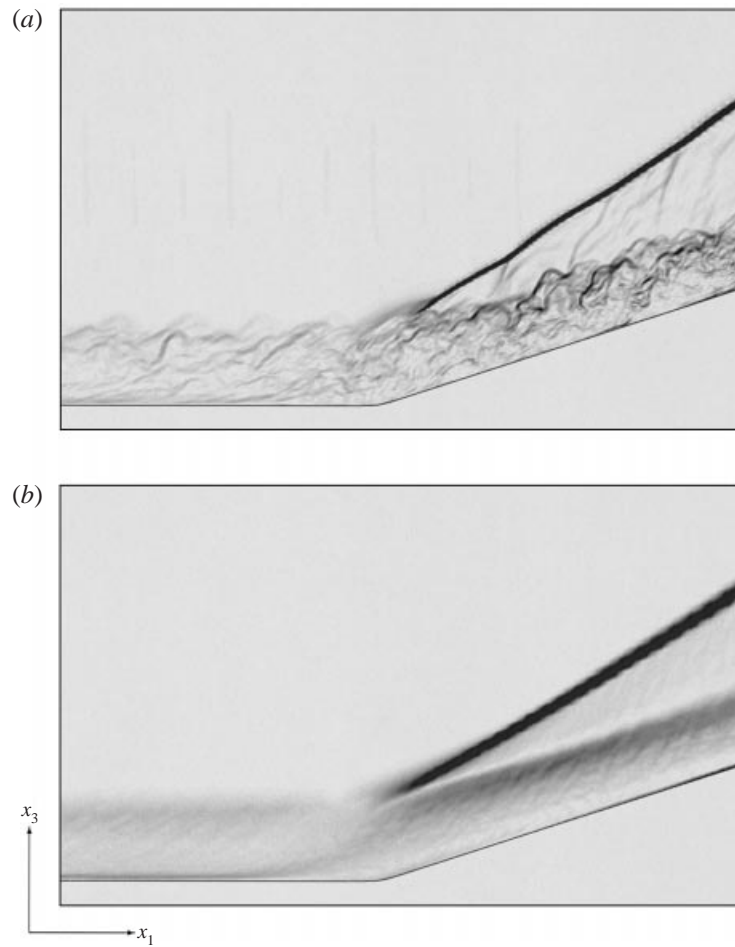
(*a*)

(*b*)

x_3

x_1

FIGURE 9. Flow-field Schlieren imitation, $||\nabla\rho||$ contours, (*a*) instantaneous x_2-average,
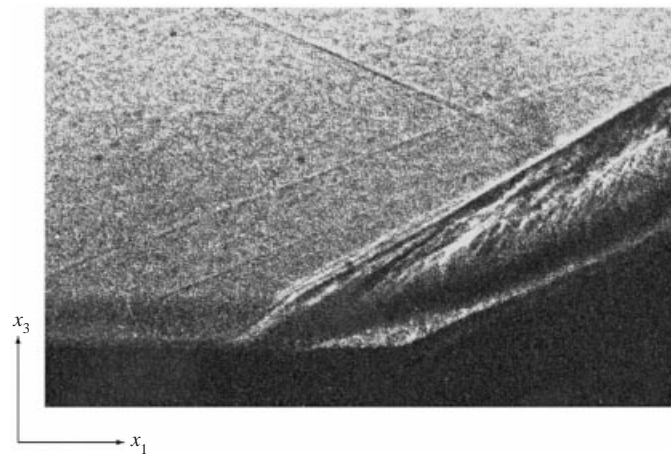(*b*) x_2-average and time average using 100 samples.

x_3

x_1

FIGURE 10. Flow-field experimental Schlieren visualization of a 25° compression ramp at
$M_\infty = 2.9$, $Re_\theta = 9600$, provided by A. Zheltovodov, ITAM, Novosibirsk.

previously mentioned wedge-like high-density zone behind the shock is clearly visible. A region with a length of about 1.5 δ_0 at the downstream edge of the computational domain is affected by the sponge outflow-boundary treatment where the boundary layer is 'cooled' down to a laminar flow, see Adams (1998).

To illustrate the shock motion, a sequence of spanwise-averaged pressure-gradient contours in (x_1, x_3)-planes is shown in figure 12. The time sequence spans a time interval of $\Delta t = 16.33$ with (almost) equal increments. The shock exhibits meandering oscillations with maximum excursions of about $0.1\delta_0$ about its mean location. No translatory or flapping motion of the shock can be observed. The shock foot penetrates, however, alternating between deeper and less deep into the boundary layer.

The dynamics of the compression shock and the separated flow around the ramp corner have been major issues in experimental research. Large-scale shock motions (LSSM) with shock excursions of the order of δ_0 were detected and investigated by Dolling & Murphy (1983). Typical shock-oscillation frequencies were found to be of the order of $0.04f_c$ to $0.07f_c$ (increasing with increasing boundary-layer thickness), where $f_c = U_\infty/\delta_0$ is the characteristic frequency of the boundary layer. This result was disputed later by Andreopoulos & Muck (1987) who report a shock-oscillation frequency of about $0.13f_c$ which they relate to the bursting frequency of the oncoming boundary layer.

To identify shock location and shock motion, Andreopoulos & Muck (1987) and Dolling & Murphy (1983) use traces of the wall pressure in the shock-foot region. We apply a similar analysis here to our numerical simulation data. In figure 13, we show time traces of the instantaneous wall pressure at x_1-positions (a) well before separation, (b) at the onset of separation, (c) within the separated region, and (d) just after reattachment, together with their normalized probability density functions (PDF). At separation, roughly in the shock-foot region, the PDF of the pressure signal flattens and develops an off-centre peak. In the separated flow, the PDF is Gaussian and just after reattachment it is slightly left-skewed. Wall-pressure signals have been measured by Dolling & Or (1985) at significantly higher Reynolds number, which allows the shock to penetrate more deeply into the boundary layer before it diffuses, as mentioned before. As a consequence, Dolling & Or (1985) report much stronger PDF-excursions from Gaussian than we observe here, although qualitative trends are similar.

Unlike the experimental data, the time traces of surface pressure do not show clearly a shock passage through the wall-pressure tracing points for our low-*Re* simulation. Having access to the full flow field we instead try to capture the shock motion directly. We place a sensor at a fixed location $x_1 = 44.88$ and $x_3 = 7.76$ ($\oplus$ in figure 12) and record the local Mach number $M(t)$ of the spanwise averaged field in time, figure 14(a). The upper curve is the local Mach number trace $M(t)$, and the lower curve is the indicator function which is $+1$ whenever $M(t)$ is larger than the mean value $\langle M \rangle$, and -1 otherwise. Similarly to Andreopoulos & Muck (1987), we can identify one shock-crossing cycle from two subsequent sign changes of the indicator function and obtain a sequence of periods from which we extract an average period $t_{sh} = 18$ with a standard deviation of stdev$(t_{sh}) = 9$. As a result, we obtain an average shock-crossing frequency at the sensor location of $f_{sh} = 0.14f_c$, which is about a factor of 2 larger than those found by Dolling & Murphy (1983) but compares well with that reported by Andreopoulos & Muck (1987). If the threshold for detecting a shock crossing is increased to $\langle M \rangle \pm 0.2$ stdev(M), where stdev(M) is the standard deviation of $M(t)$, the frequency reduces only slightly to $f_{sh} = 0.12f_c$. For thresholds $\langle M \rangle \pm 0.5$ stdev(M) or $\langle M \rangle \pm$ stdev(M) it drops to $f_{sh} = 0.08f_c$ and $f_{sh} = 0.05f_c$, respectively.
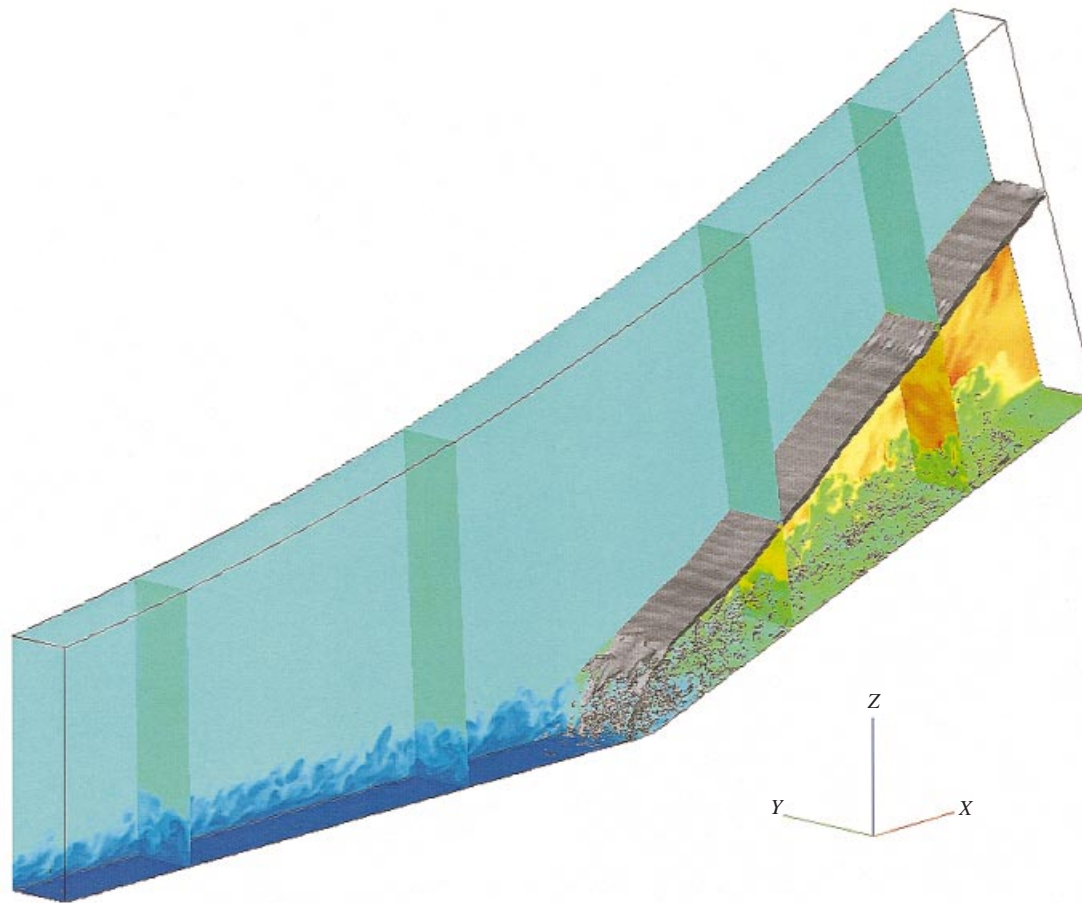
FIGURE 11. Density at the wall, in the plane $x_2 = 2.9$ and 4 crossflow planes; shock-surface with $\partial_{x_i} u_i = -0.4$; high density: red; low density: blue; solid black lines indicate the computational-domain boundaries.
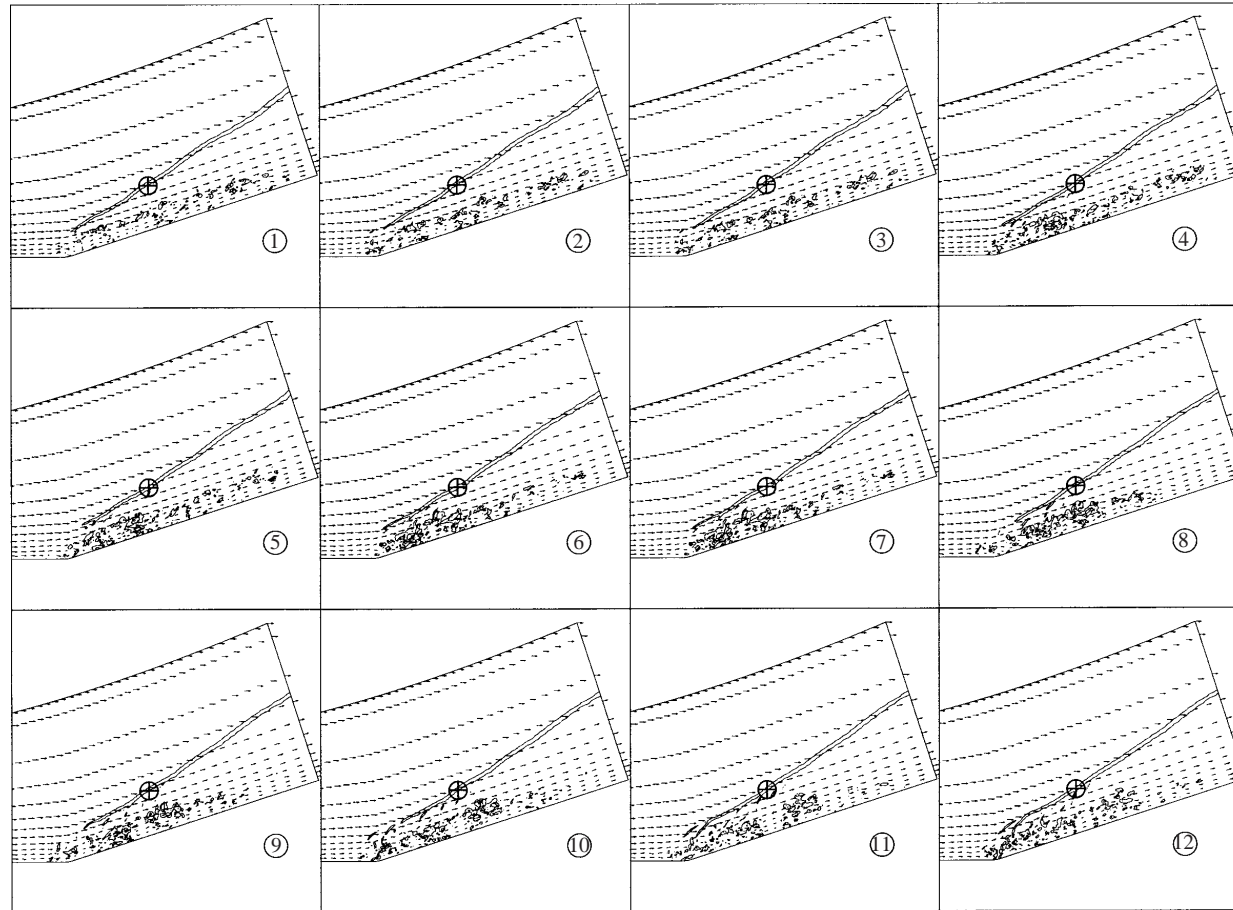
FIGURE 12. Sequence of shock evolution (iso-contours of $||\nabla p||$) and velocity vectors at $x_2 = 0.72$ for a sequence of equal timesteps between $t_l = 309.00$ and $t_r = 325.34$; sequence from bottom to top and left to right (numbers 1 to 12); the marker indicates the sensor position for figure 14; flow direction is from bottom up.
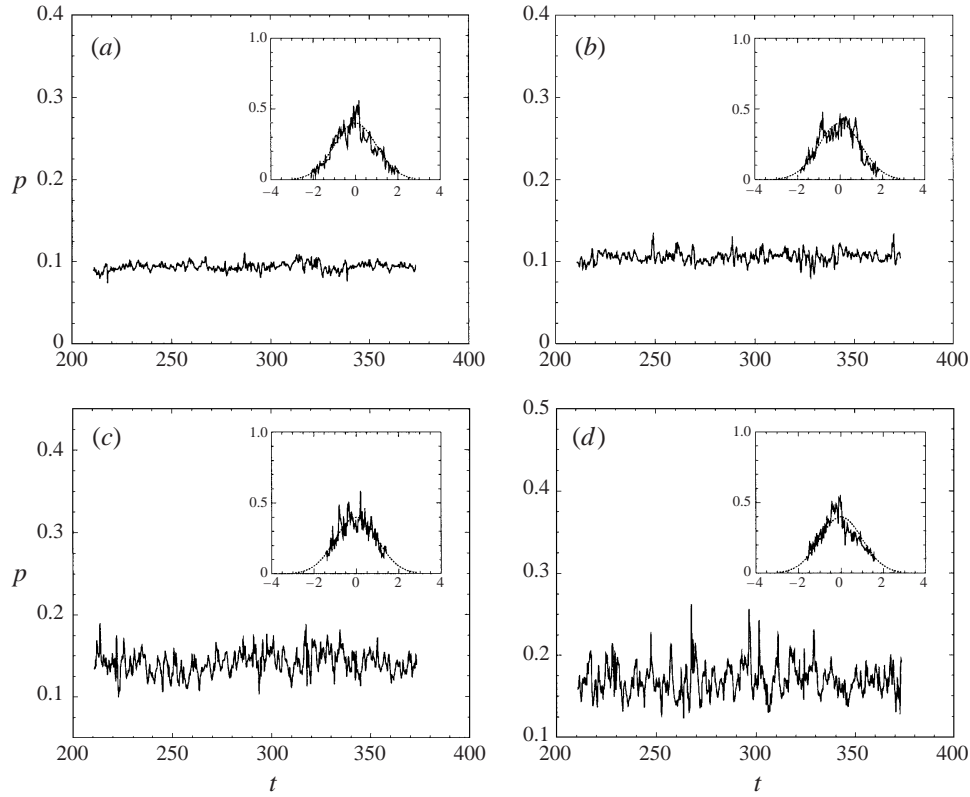
FIGURE 13. Wall-pressure traces at positions (*a*) $x_1 = 31.6$, (*b*) $x_1 = 32.8$, (*c*) $x_1 = 35.0$, (*d*) $x_1 = 36.4$, in the plane $x_2 = 0$; normalized PDF in inset, dotted line is a Gaussian distribution, for reference.
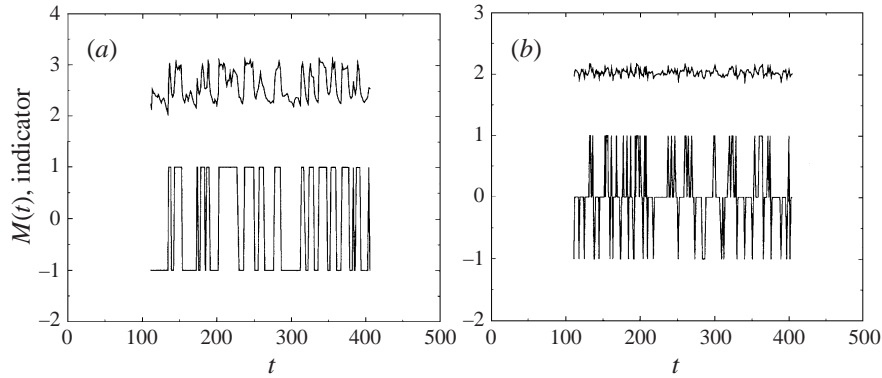
FIGURE 14. (*a*) Mach-number traces and shock indicator at $x_1 = 44.88$ and $x_3 = 7.76$, (*b*) Mach-number traces and burst indicator at $x_1 = 8.62$ and $x_3 = 1.27$.

To find out whether the shock motion is driven by bursting events (i.e. the sequence of an ejection of near-wall fluid into the outer flow followed by a sweep of outer fluid), we perform a similar analysis in the oncoming boundary layer. Figure 14(*b*) shows a recorded $M(t)$ trace at a point ($x_1 = 8.62$, $x_3 = 1.27$), well upstream of the interaction zone within the oncoming boundary layer. $M(t)$ can be related to turbulent bursting events, since an ejection of low-speed high-temperature near-wall

fluid appears as a low-Mach-number spot within the ambient low temperature and high-speed outer fluid. We set an indicator to ± 1 whenever the Mach number exceeds or falls below the average by an amount of one standard deviation of the recorded data; otherwise it is 0. The bursting frequency is the inverse of the average delay time between two subsequent bursting events. Given the above mentioned relation between local Mach number and bursting events, it can be estimated from the time between two subsequent sign changes of the indicator function. This procedure gives a frequency of $f_b = 0.13 f_c$, which happens to be very close to f_{sh}. However, the large standard deviations of the signals in both cases should be considered, for f_b it is $\mathrm{stdev}(f_b) = 0.08 f_c$. Yet, since both procedures give at least similar magnitudes, we conclude that the proposition of Andreopoulos & Muck (1987) which states that turbulent bursting events drive the shock motion is quite plausible in our case. For the low Reynolds number of our data, the value f_b compares well with the bursting frequency reported for incompressible boundary layers by Blackwelder & Haritonidis (1983). The shock dynamics depends on the unsteady deformation of the sonic layer. Also, it depends on the unsteadiness of the supersonic flow above the sonic layer which the compression waves radiating from the sonic layer have to pass. Accordingly, the coupling between shock motion and the events which trigger compression waves or change their medium is quite complex and does not necessarily exhibit a clear phase-locking. The mere fact, however, that shock oscillation and bursting happen at similar frequency indicates a close connection between them.

Unsteady large-scale streamwise vortices have been suggested as one possible origin for low-frequency LSSM (Smits & Dussauge 1996). The Görtler number for a turbulent flow can be estimated as

$$G_T = \frac{\theta}{0.018\delta_1} \sqrt{\frac{\theta}{R}},$$

(Smits & Dussauge 1996, p. 277), where R is the curvature radius of the average streamlines within the boundary layer close to the corner, θ is the momentum thickness and δ_1 the displacement thickness. From the simulation data, a maximum of $G_T = 6$ can be estimated roughly, which is slightly less than the critical Görtler number for a laminar flow. For that reason, we expect Görtler instability to be weak. In our case, we did not find indications for the presence of large-scale streamwise vortices. It should be noted, however, that the spanwise extent of the computational domain, $L_2 \simeq 1.2\delta_0$, does not allow for the resolution of Görtler vortices since their spacing is typically about $2\delta_0$. It also has been found by Smits & Muck (1987) that for a case of incipient separation ($\beta = 16°$ and $M_\infty = 3$) the large-scale flow exhibits an overall two-dimensionality. For higher deflection angles and thus larger separation, Smits & Muck (1987) concluded the presence of longitudinal roll cells from surface streak patterns.

To investigate the separation dynamics further, we study the time behaviour of the spanwise-averaged skin-friction coefficient. A negative skin-friction coefficient is necessarily associated with a local region of backflow. This we take here synonymously with a separated flow, avoiding the issue of how to define unsteady separation properly. Figure 15 shows a time trace of the x_1-location where the spanwise-averaged skin friction becomes negative first (lower curve) and a time trace of the location where the skin friction becomes positive again last (upper curve). Unlike what was found in our preliminary simulations (Adams 1997), owing to the different inflow conditions, there is no dominant frequency on the order of f_c in the Fourier transform of the signals (see inset of figure 15). The very low-frequency mode with $f \simeq 0.006$ is a remnant
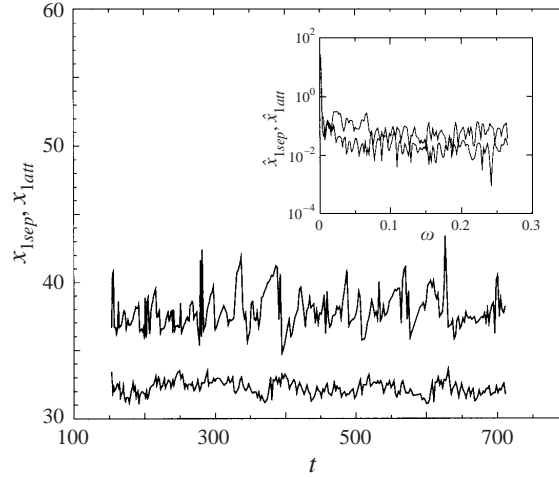
FIGURE 15. Time trace of spanwise-averaged separation and reattachment line (as defined in the text), Fourier decomposition in the inset.

of the inflow treatment, where data repeat with about that frequency. Otherwise, the spectrum is broadband and there is no visible correlation between separation-line and reattachment-line oscillation, from which we conclude that upstream communication is insignificant in our case. It should be noted, however, that Smits & Dussauge (1996) suggest an upstream communication across the area of separated flow to explain a coupling between separation and reattachment line dynamics which has been observed by Dolling & Murphy (1983).

3.5. Turbulence structure

Some of the most significant turbulent correlations are Reynolds stresses, auto-correlations and individual terms of the transport equation for turbulent kinetic energy. From experiments and theory, it is known that turbulent fluctuations are amplified and auto-correlations and Reynolds shear stresses increase across the interaction (the latter holds strictly only for sufficiently oblique shocks). Owing to the parameter differences between our DNS and available experiments, differences in the mean flow result, which has been pointed out before, and we cannot expect a quantitative agreement with the experimental data. Trends and amplifications rates are, however, in reasonable agreement with the experiments. The root mean square (RMS) of mass-flux fluctuations $(\rho u_1^c)' = \rho u_1^c - \overline{\rho u_1}^c$ increases from a maximum of 0.09 in the oncoming boundary layer at station 1 to a maximum of 0.43 at station 10, figure 16(a). The amplification factor of 4.8 compares reasonably well with the range found by Smits & Muck (1987). The main contribution to the mass-flux amplification comes from the density fluctuations, compare figures 16(b) and 16(c). Whereas velocity fluctuations are maximum in the area of separated flow and then decay, density fluctuations continue to rise behind the shock. The magnitude of the temperature fluctuations $T'' = T - \tilde{T}$ is less affected by the interaction, figure 16(d), and RMS(T'') rises from a maximum of about 0.2 to about 0.3.

The Reynolds normal stress $\tau_{11} = \overline{\rho u_1'' u_1''}$, the Reynolds shear stress $\tau_{13} = \overline{\rho u_1'' u_3''}$, and the Reynolds heat flux $\tau_{h3} = \overline{\rho u_3'' T''}$, as shown in figure 17, are rotated into a coordinate system which is aligned with the wall (superscript $\perp$). This transformation agrees with the way experimental data are shown usually, since measurement probes
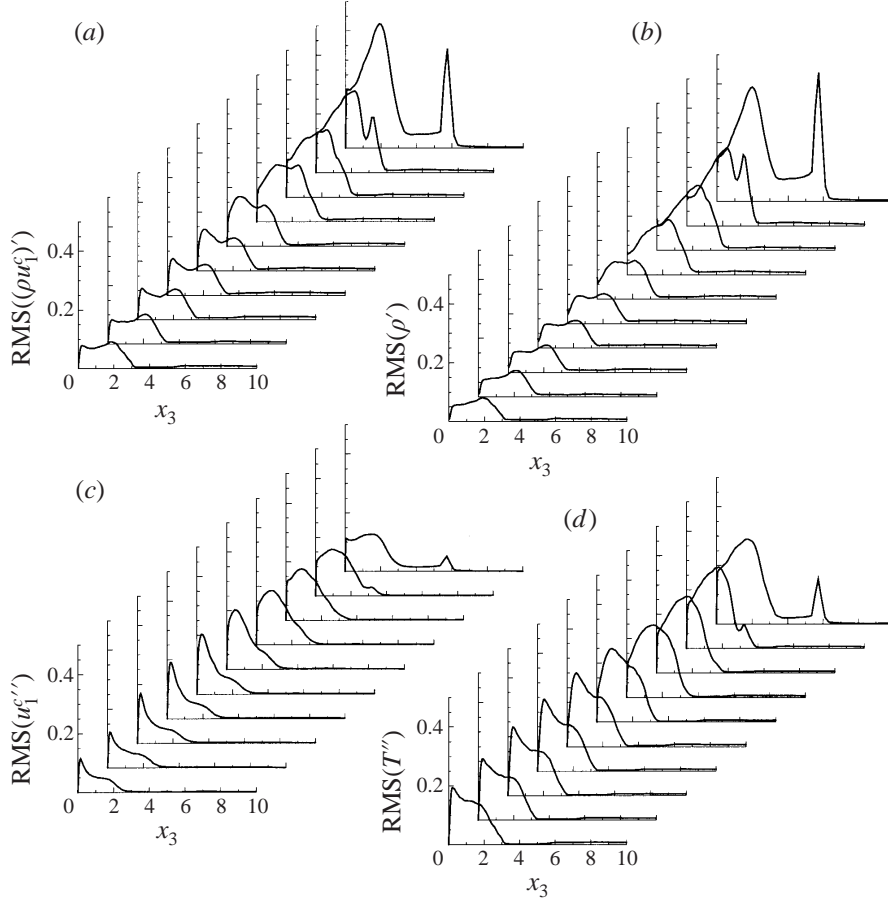
FIGURE 16. (*a*) RMS$((\rho u_1^c)')$, (*b*) RMS(ρ'), (*c*) RMS$(u_1^{c\prime\prime})$ and (*d*) RMS(T'') at downstream stations 1–10 according to figure 2.

are aligned with the wall. The maximum Reynolds normal stress is amplified by a factor of about 4 the maximum of the Reynolds shear stresses by a factor of about 13, figures 17(*a*) and 17(*b*). The experimental data of Smits & Muck (1987) show amplification factors of about 5 to 7 and 6 to 12, respectively, the lower values for $\beta = 16°$ and the higher for $\beta = 20°$. If we follow the DNS data along a mesh line, which roughly corresponds to following a mean streamline, instead of picking the maximum of the respective profiles before and behind the shock we obtain a maximum amplification of about 13 for the normal stress and of about 14 for the shear stress. A comparable amplification has been observed by Smits & Muck (1987) when the measurements followed a mean-flow streamline. The maximum of the Reynolds heat flux is amplified by about a factor of 4 (figure 17*c*), whereas following a coordinate line we find a maximum amplification factor of about 8.

A direct comparison of the computed profiles for $\tau_{11}^{\perp}$ and $\tau_{13}^{\perp}$ with the experimental data ExpB and ExpC confirms that amplification rates and qualitative evolution are similar, with obvious differences due to the less pronounced upstream effect of the pressure gradient at the higher experimental Reynolds numbers, figure 18. It should also be noted that $\tau_{13}^{\perp}$ is quite sensitive to the coordinate transformation. Close to the corner, $\tau_{13}^{\perp}$ and τ_{13}^c can differ by 50%. For the experimental data, a similar sensitivity to the probe alignment can be expected.
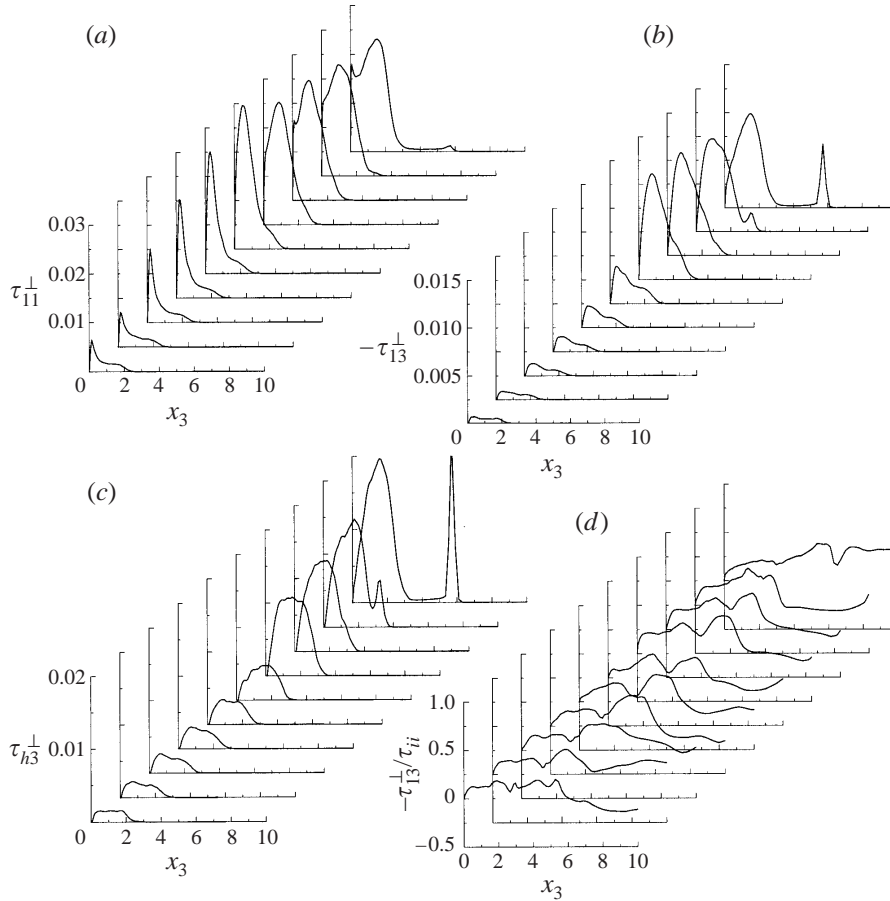
FIGURE 17. (a) $\tau_{11}^{\perp}$, (b) $-\tau_{13}^{\perp}$, (c) $\tau_{h3}^{\perp}$, and (d) $a = -\tau_{13}^{\perp}/\tau_{ii}$ at downstream stations 1–10 according to figure 2.

The downstream evolution of the specific Reynolds normal stress $\overline{u_1''u_1''}$ and the specific Reynolds shear stress $\overline{u_1''u_3''}$ are compared with the experimental data ExpB and ExpC in figure 19. Whereas the experimental data show a sudden increase of the maxima of the $\overline{u_1''u_1''}$ and $\overline{u_1''u_3''}$ profiles (hollow symbols) behind the corner, the simulation indicates a peak before the corner (filled symbols). The lines show the respective distributions along mesh lines at different distances above the wall. The maxima move downstream with increasing distance from the wall. If the amplification of the maxima for the simulation data and for the experimental data are compared, the agreement (aside from the location) is good. Since the measurements do not resolve the near-wall region well, the downstream shift of the maximum specific Reynolds stresses with increasing distance from the wall can lead to an underestimation of amplification rates in the experimental data.

The trends for the evolution of Reynolds stresses across the interaction agree with those predicted by rapid distortion theory (RDT) (Mahesh et al. 1993). It has been noted however, that RDT gives rather too small a stress amplification. Different amplification of the shear and the normal components leads to a change of the structure parameter $a = -\tau_{13}^{\perp}/\tau_{ii}$ shown in figure 17(d). In the oncoming boundary layer, a increases from 0.12 to about 0.17 towards the boundary-layer edge, which agrees well with data reported for incompressible boundary layers (Smits & Dussauge
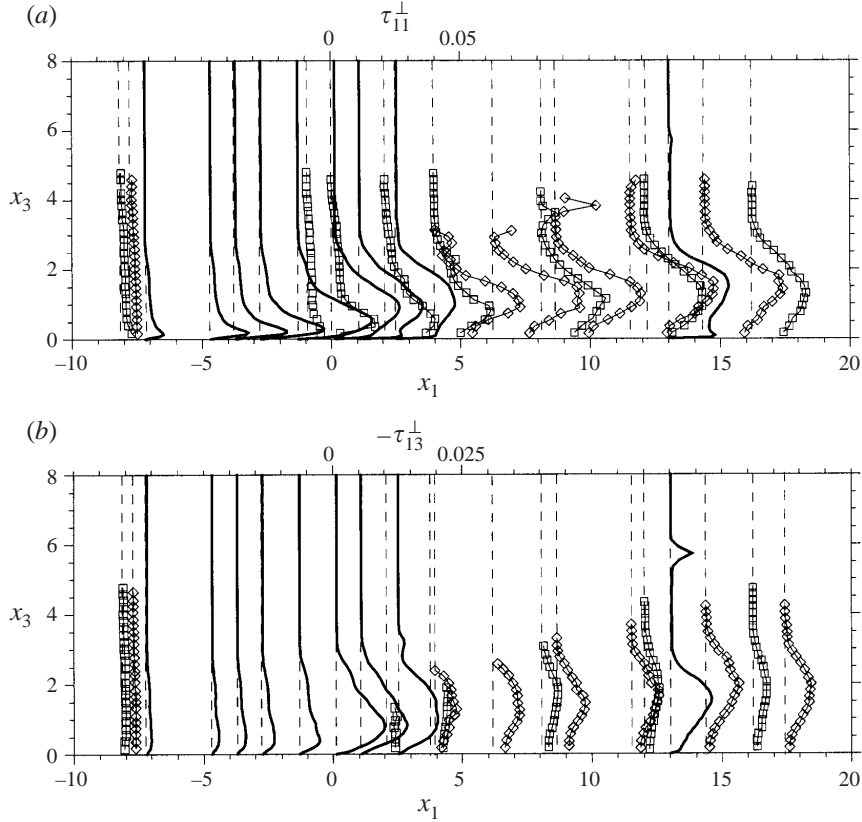
FIGURE 18. Downstream evolution of Reynolds-stress profiles: (a) $\tau_{11}^\perp$, (b) $-\tau_{13}^\perp$; ——, simulation data; $\square$, ExpB; $\diamondsuit$, ExpC; thin dotted vertical lines are the reference lines for the respective profiles, which give the downstream position x_1 from the ramp corner (lower horizontal axis) and from which the magnitude of $\tau^\perp$ is measured (upper horizontal axis).

1996, p. 215). Through the interaction region, a increases to values of about 0.35 in the outer part of the boundary layer. Well downstream of reattachment, a decreases towards its magnitude prior to the interaction (station 10).

A fundamental equation of turbulence modelling is the transport equation for turbulent kinetic energy which can be written according to Gatski (1997) as:

$$\underbrace{\frac{\partial \bar{\rho}K}{\partial t} + \frac{\partial}{\partial x_j}(\tilde{u}_j\bar{\rho}K)}_{I} = \underbrace{\bar{\rho}\tilde{\mathscr{P}}}_{II} + \underbrace{\bar{\rho}\Pi^d}_{III} + \underbrace{\mathscr{M}}_{IV} + \underbrace{\frac{\partial \tilde{\mathscr{D}}_j^t}{\partial x_j}}_{V} - \underbrace{\bar{\rho}\varepsilon}_{VI} + \underbrace{\frac{\partial}{\partial x_j}\left(\frac{\bar{\mu}}{Re}\frac{\partial K}{\partial x_j}\right)}_{VII}, \qquad (3.3)$$

where the turbulent kinetic energy (TKE) is defined as

$$K = \tfrac{1}{2}\bar{\rho}\widetilde{u_i''u_i''}.$$

The following definitions and interpretations are assigned to the individual terms of equation (3.3):

(I) is the convection of K;

(II) is the production of K

$$\bar{\rho}\tilde{\mathscr{P}} = -\bar{\rho}\widetilde{u_i''u_j''}\frac{\partial \tilde{u}_i}{\partial x_j};$$
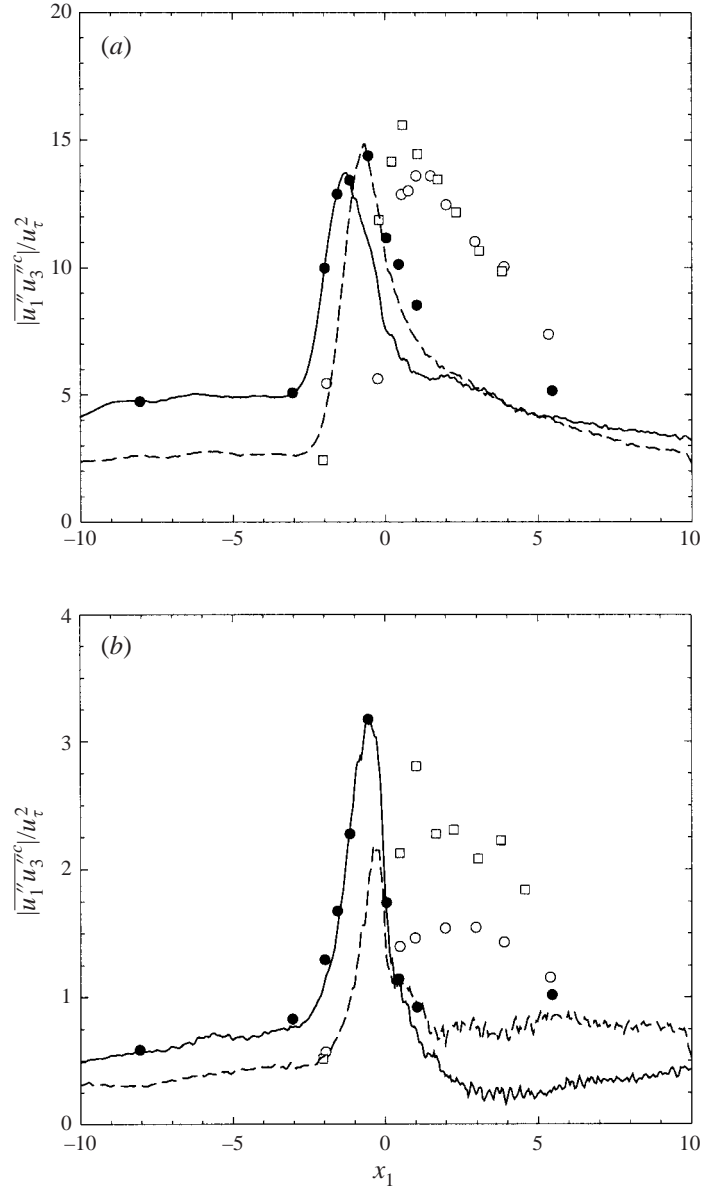
FIGURE 19. (*a*) Specific Reynolds normal stress $\overline{u_1'' u_1''}^{c}$, (*b*) specific Reynolds shear stress $|\overline{u_1'' u_3''}^{c}|$, normalized with the friction velocity at the inflow u_τ^2; O, ExpB; □, ExpC; DNS: ●, maximum values over x_3, (*a*) ——, along mesh line starting at $x_1^+ = 10$; - - -, along mesh line starting at $x_1^+ = 25$, (*b*) ——, along mesh line starting at $x_1^+ = 25$, - - -, along mesh line starting at $x_1^+ = 59$; experimental data were taken from Fernholz *et al.* (1989).

(III) is the pressure dilatation

$$\bar{\rho} \Pi^d = \overline{p' \frac{\partial u_k'}{\partial x_k}},$$

which is a purely compressible term since it vanishes for divergence-free flows;

(IV) is the mass flux variation

$$\mathscr{M} = \overline{u''}_i \frac{\partial \bar{\tau}_{ij}}{\partial x_j} - \overline{u''}_i \frac{\partial \bar{p}}{\partial x_i},$$

where the last term is often considered separately and denoted as the pressure-work term Π^W;

(V) is the turbulent diffusion

$$\frac{\partial \tilde{\mathscr{D}}_j^t}{\partial x_j} = -\frac{\partial}{\partial x_j} \left[\frac{1}{2} \bar{\rho} \widetilde{u_i'' u_i'' u_j''} + \overline{p' u_j'} \right];$$

(VI) is the turbulent dissipation

$$\bar{\rho} \varepsilon = \overline{\tau_{ij}' \frac{\partial u_i'}{\partial x_j}} = \varepsilon^s + \varepsilon^d,$$

where

$$\varepsilon^s = \frac{\bar{\mu}}{Re} \overline{\left(\frac{\partial u_i'}{\partial x_j} - \frac{\partial u_j'}{\partial x_i} \right)^2}, \quad \varepsilon^d = \frac{4}{3} \frac{\bar{\mu}}{Re} \overline{\left(\frac{\partial u_i''}{\partial x_i} \right)^2}, \quad \varepsilon^i = 2 \frac{\bar{\mu}}{Re} \left(\frac{\partial \overline{u_i' u_j'}}{x_i x_j} - 2 \frac{\partial}{\partial x_i} \overline{u_i' \frac{\partial u_j'}{\partial x_j}} \right)$$

(Huang, Coleman & Bradshaw 1995). ε^d is the dilatational dissipation, which is the other purely compressible term in equation (3.3) since it disappears with the trace of $\partial u_i / \partial x_j$;

(VII) is the viscous diffusion.

It should be noted that correlations involving viscosity fluctuations have been neglected in the definitions of terms VI and VII. They are certainly unimportant in the present case, see also Huang *et al.* (1995).

As a main indicator for compressibility effects, the turbulent Mach number is often used and is defined as

$$M_t = \frac{\sqrt{2K/\bar{\rho}}}{\bar{a}} \tag{3.4}$$

($\bar{a}$ is the mean speed of sound).

The maximum of K increases by about a factor of 4 (figure 20*a*). M_t assumes a maximum of about 0.5 in the interaction area, rising from about 0.25 (figure 20*b*). The rather high value of M_t indicates potentially significant compressibility effects in the interaction area. This issue is addressed in §3.6. A comparable value of M_t has been found in flat-plate boundary layers at $M_\infty = 4.5$ and $M_\infty = 6$ (Maeder *et al.* 2000). There, however, the genuinely compressible contributions in equation (3.3) were found to be small.

In figure 21, we display the most significant terms of equation (3.3) which are not genuinely compressible. Correlations involving fluctuation gradients and pressure fluctuations lack smoothness owing to the limited number of samples. To obtain smoother statistics for these quantities, up to twice as many samples would be required, which we found impractical considering the computational cost of the present simulation. We refrain from post-processing filtering as was proposed by Na & Moin (1996) to improve the legibility of the data. Production $\bar{\rho} \tilde{\mathscr{P}}$ increases during the interaction. Whereas, in the oncoming boundary layer, $\bar{\rho} \tilde{\mathscr{P}}$ is maximum near the wall, the maximum detaches from the wall, and, further downstream, the $\bar{\rho} \tilde{\mathscr{P}}$ profile resembles that of a wake-flow (e.g. Moser, Rogers & Ewing 1998). The wake-like
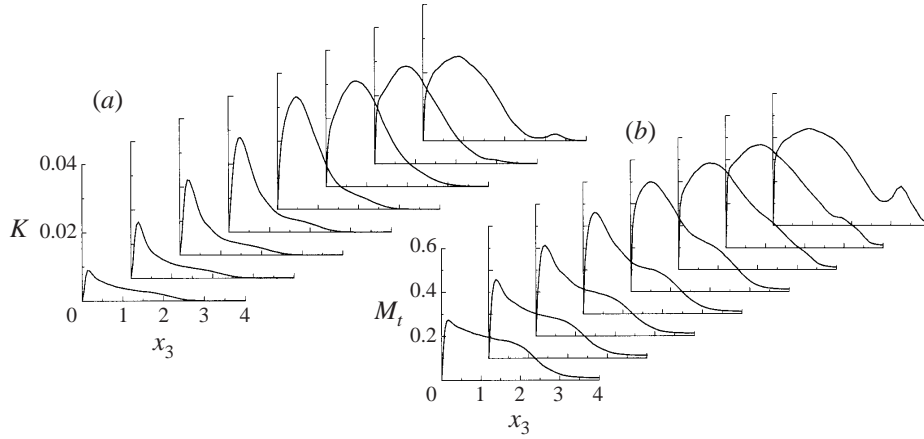
FIGURE 20. (*a*) Turbulent kinetic energy K, (*b*) turbulent Mach number M_t at downstream stations 2–9, according to figure 2.

Station	λ	Re_λ	x_3
1	0.22	47	1.96
2	0.23	54	2.33
3	0.23	54	2.42
4	0.23	58	2.46
5	0.24	68	2.49
6	0.24	91	2.55
7	0.25	145	2.59
8	0.24	169	2.58
9	0.24	205	2.58
10	0.26	326	2.54

TABLE 4. Taylor microscale and microscale Reynolds number along a mesh line starting at $x_1 = 0$ and $x_3^+ = 91$ (referring to inflow) for the downstream stations 1–10, also given are the respective distances from the wall.

shape of the mean velocity profiles downstream of the interaction is evident from figure 5(*a*). Along with increased fluctuation levels the dissipation $\bar{\rho}\varepsilon$ also increases. Near the wall, a steep increase of velocity fluctuations at the wall causes a large dissipation magnitude. Pressure diffusion and pressure work assume a considerable magnitude in the vicinity of the shock.

Table 4 shows the variation of the Taylor microscale and the microscale Reynolds number across the interaction. The distribution follows a mesh line which starts at $x_3^+ = 97$ at inflow. The Taylor microscale is computed from

$$\lambda^2 = -\frac{1}{R''_{u_1,u_1}} \tag{3.5}$$

where R''_{u_1,u_1} is the second derivative at $\delta_{x_2} = 0$ of the two-point auto-correlation function R_{u_1,u_1}, as shown in figure 4. The small variations of λ are mainly due to the slightly varying distance from the wall when following a mesh line. The increase in Re_λ is a local Reynolds-number effect due to increasing density.
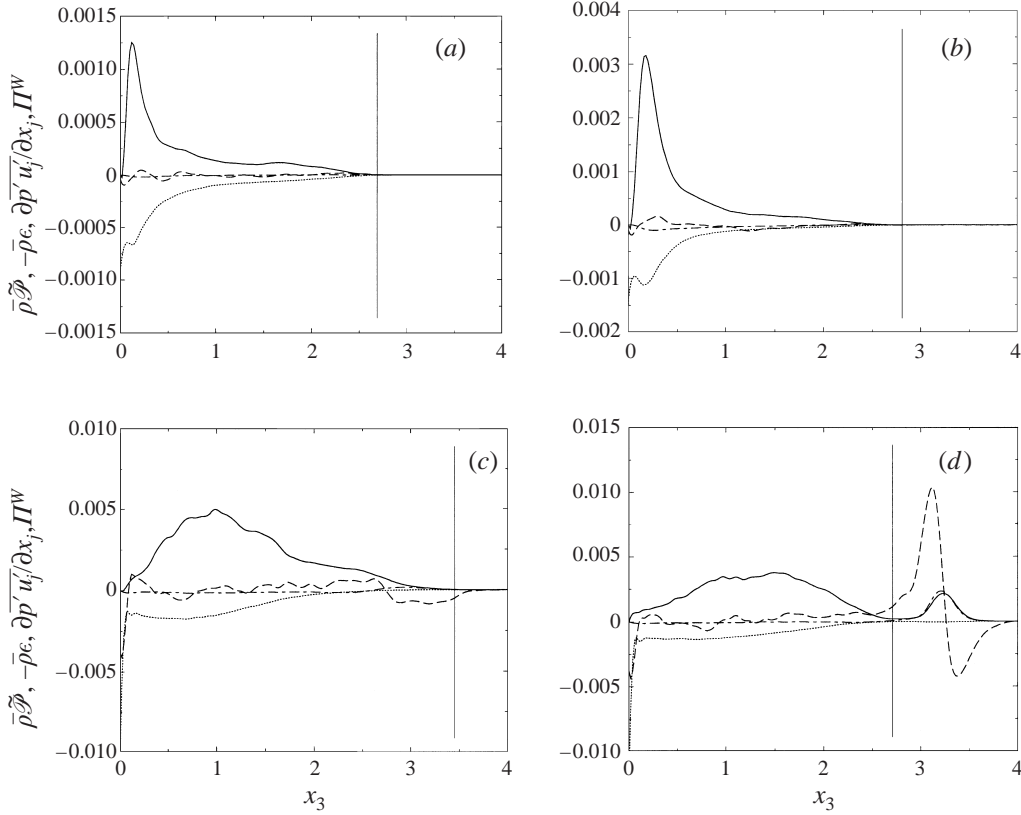
FIGURE 21. Turbulent kinetic energy balance, ——, production $\bar{\rho}\tilde{\mathscr{P}}$; ......, turbulent dissipation $\bar{\rho}\varepsilon$; — — — —, pressure diffusion $\partial\overline{p'u'_j}/\partial x_j$; — · —, pressure work Π^W; (a) station 2, (b) station 4, (c) station 7, (d) station 9; the vertical solid line indicates the 99% local mean boundary-layer thickness.

3.6. *Compressibility effects*

Owing to flow compressibility, two additional terms appear in the balance equation for K (3.3), the pressure dilatation Π^d and the dilatational dissipation ε^d. In homogeneous turbulence, their magnitude has been shown to be related to the magnitude of the turbulent Mach number, (see e.g. Blaisdell, Mansour & Reynolds 1993). More recently, Ristorcelli (1997) showed that under certain formal restrictions and in the case of small M_t^2, pressure dilatation scales with M_t^2. Dilatational dissipation scales with M_t^4 and is inversely proportional to the turbulent Reynolds number. Ristorcelli (1997) also noted that Π^d is large in non-equilibrium areas of the flow.

For our results, ε^d is overall smaller than Π^d by about one order of magnitude, figure 22. Within the boundary layer, ε_d is about two orders of magnitude smaller than the total dissipation ε throughout the interaction area (note that ε^d as shown in figure 22 is multiplied by a factor of 10). $\bar{\rho}\Pi^d$ assumes a significant magnitude near the wall and around the shock foot, figure 22(d). In the shock foot, $\bar{\rho}\Pi^d$ is larger than production by a factor of 2, and dissipation is small. The dominant contribution in the shock-foot area comes from pressure diffusion. It should again be pointed out that at higher Reynolds number the shock foot penetrates more deeply into the boundary layer. Then production of K within the boundary layer rises, and an increased redistribution between internal energy and TKE is to be expected.
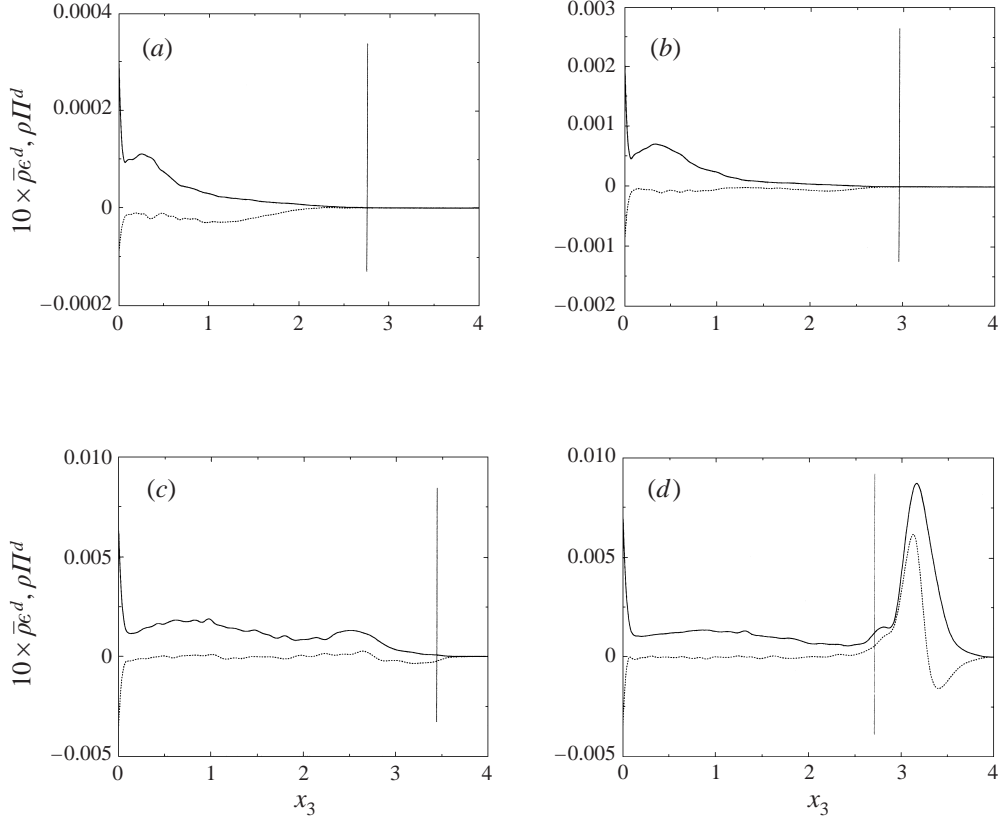
FIGURE 22. Turbulent kinetic energy balance, ——, dilational dissipation $10 \times \bar{\rho}\varepsilon^d$ (scaled by a factor of 10); ......, pressure dilatation $\bar{\rho}\Pi^d$; (a) station 2, (b) station 4, (c) station 7, (d) station 9; the vertical solid line indicates the 99% local mean boundary-layer thickness.

Mahesh et al. (1997) found that the strong Reynolds analogy (SRA), which can be derived from Morkovin's hypothesis (Lele 1994), is not satisfied for isotropic turbulence interacting with a normal shock. For an assessment of the strict form of the SRA we show profiles of the velocity–temperature correlation

$$R_{u_1,T} = -\frac{\overline{u_1^{c\prime}T'}}{\sqrt{\overline{u_1^{c\prime}u_1^{c\prime}}}\sqrt{\overline{T'T'}}} \tag{3.6}$$

in figure 23. At the first station, the $R_{u_1,T}$ profile is typical for zero-pressure-gradient boundary layers (Maeder et al. 2000). In the logarithmic region, $R_{u_1,T}$ reaches a maximum of about 80%. It diminishes to about 60% in the outer part and then drops rapidly to zero at the boundary-layer edge. The behaviour in the outer part of the boundary layer persists downstream. In the area of mean-separated flow near the wall, the correlation as defined in equation (3.6) is negative. During the interaction, $R_{u_1,T}$ is significantly less than 50% in the major part of the boundary layer. It does not exceed this value downstream of the interaction. Near the shock-foot, $R_{u_1,T}$ varies strongly. It first rises to about 90% and then drops steeply to about 20% just above the shock-foot. The quantitative implications of this behaviour in the interaction and in the recovery region on experimental data acquisition remain to be assessed. In any
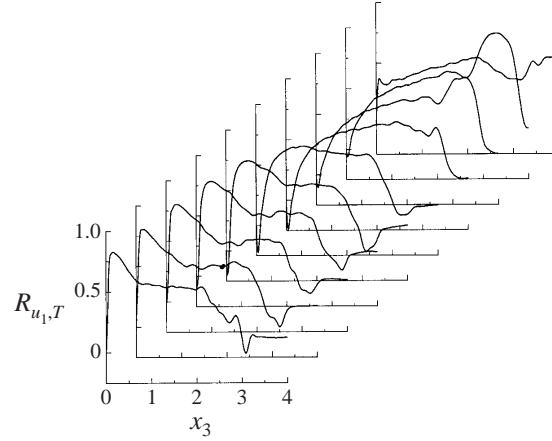
FIGURE 23. Profiles of $R_{u_1,T}$ at stations 1–10.

case, less than 50% correlation makes the justification of an *a priori* assumption of SRA questionable.

Vorticity generation is one of the most important turbulence production sources. For incompressible flow, it is the only source; for compressible flows, turbulence can also be driven by fluctuations of the thermodynamic state. As mentioned above, in our case, the flow is rather dominated by a solenoidal behaviour, with some exceptions in regions of high-turbulence non-equilibrium. The question arises, whether in these regions vorticity is mainly generated by stretching and tilting of vorticity, which is a solenoidal vorticity generation mechanism, or whether the baroclinic production contributes significantly. Baroclinic production has been found to play a major role when entropy fluctuations interact with a normal shock (Mahesh *et al.* 1997).

Neglecting diffusion (for simplicity) the transport equation for the mass-weighted vorticity ω_i/ρ can be written as

$$\frac{\partial \omega_i/\rho}{\partial t} + u_j \frac{\partial \omega_i/\rho}{\partial x_j} = \underbrace{\frac{\omega_j}{\rho} \frac{\partial u_i}{\partial x_j}}_{I_i} + \underbrace{\frac{1}{\rho^3} \epsilon_{ijk} \frac{\partial \rho}{\partial x_j} \frac{\partial \rho}{\partial x_k}}_{II_i}, \tag{3.7}$$

where I is the production by stretching and tilting and II is the baroclinic production.

We display the ensemble-averaged spanwise component $\bar{I}_2$ and $\overline{II}_2$ of these terms in a region around the corner in figure 24. Note that our nomenclature implies that $\bar{\omega}_2$ is positive owing to the mean shear-rate, and positive contributions $\bar{I}_2$, $\overline{II}_2$ increase ω_2. Stretching production is dominant near the wall in the small mean-separated area ahead of the corner. Only around and beneath the shock-foot area does baroclinic production reach an appreciable magnitude. It can be expected that baroclinic vorticity production would affect turbulence structure more significantly if the shock penetrates further into the boundary layer, at higher Reynolds numbers, for instance (Mahesh *et al.* 1997). Outside the boundary layer, vorticity production across the shock is insignificant since the ambient fluid has only small fluctuations. It should be noted that terms $\bar{I}$ and $\overline{II}$ are formally singular at the shock. To avoid spurious oscillations, derivatives across the shock have been computed with an essentially non-oscillatory (ENO) interpolation during the post-processing stage.
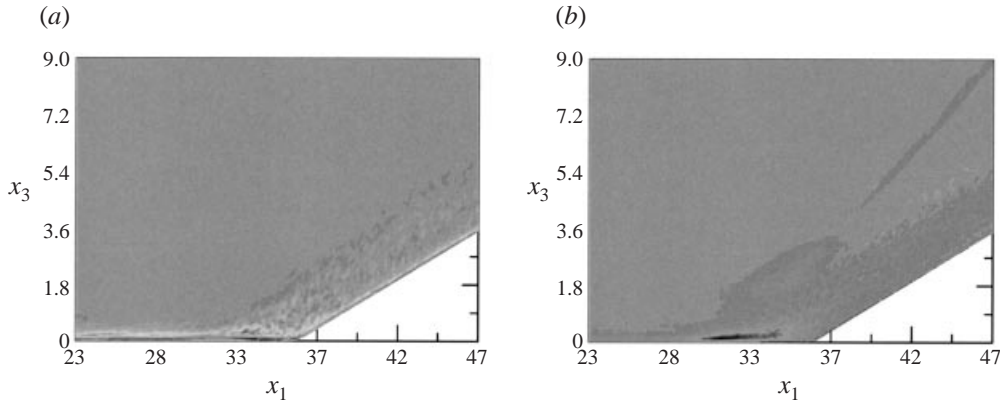
FIGURE 24. (a) Stretching production term $\bar{I}_2$, (b) baroclinic production term $\overline{II}_2$; 8 grey-scale levels in the range $-0.03 \leqslant \overline{II} \leqslant 0.06$ (light to dark).

4. Discussion

There are two possible sources for the disagreement between results reported for RANS computations using turbulence models and experimental results. First, experiments often (in particular for large separations) show an unsteady large-scale shock motion (LSSM) which is apparently not related to turbulence events in the oncoming boundary layer. The origin of this behaviour is unclear, it may be caused by a low-frequency instability of large-scale cross flow structures, such as unsteady Görtler vortices. It also may be that these LSSMs are driven by variations in the oncoming flow or in the ambient flow. If there is a LSSM then the meaning of a time-averaged RANS solution becomes unclear. This point has been addressed by Marshall & Dolling (1992) with the recommendation that an inclusion of LSSM is likely to be essential to improve RANS predictions in relevant cases. If LSSM has an origin within the interaction area this should be captured by the turbulence model. In our case, we did not observe any LSSM. The spanwise extent of the computational domain being insufficient to capture relevant large-scale cross flow vortex structures is a possible reason, but not a likely reason at our flow parameters, considering that no evidence for their existence was found in our simulation and the rather low estimated Görtler number. When considering LSSM, one should be aware that the shock-separation dynamics is very sensitive to events in the oncoming flow. A forcing in the inflow data reflects clearly in the unsteady behaviour of the separation location and the shock. We expect that large-eddy simulations which should be able to reach to significantly higher Re and domain sizes in the near future will help to clarify this point.

A second candidate for a disagreement between turbulence-model predictions and experimental data is the effect of compressibility. The shock-foot region is a source of turbulence production and of enhanced compressibility effects, which are expressed by an increased pressure dilatation. It is found that dilatational dissipation is insignificant. Pressure dilatation reaches an appreciable magnitude only in the small region of separated flow and around the shock-foot, but is small otherwise. Concerning turbulence statistics we can therefore conclude that compressibility has no major effect on them. Again, it should be noted that this may be quite different at higher Reynolds numbers since the flow structure changes on the large-scales and the shock-foot penetrates more deeply into the boundary layer. An obvious compressibility effect which is

not directly related to the turbulence structure is the shock-induced density increase. The shock-foot is the origin of a wedge-like region of high density extending downstream. Yet, turbulence adjusts fast enough for it to behave as dominantly solenoidal in this region.

Smits & Muck (1987) point out that a number of mechanisms acting individually or simultaneously can be responsible for amplification of turbulence activity across a shock–boundary-layer interaction. The first to consider is the interaction of shear-driven turbulence with an oblique rapid distortion due to very large flow gradients across a shock (in an integral sense, the Rankine–Hugoniot conditions), see Mahesh *et al.* (1996) and Lele (1992*b*). In our case, the pressure gradient which is felt by the turbulence within the boundary layer is more gradual, since the shock does not penetrate deeply into the boundary layer. As has been observed in experiments (Spin *et al.* 1994), a more gradual streamline curvature of a few δ_0 can cause a similar amplification to a sudden deflection, when flow states sufficiently far upstream and downstream of the interaction area are compared. The ratio between turbulent timescale and distortion timescale can be estimated as

$$\frac{\overline{u_i' u_i'}}{\lambda} \frac{L_{up}}{U_\infty} = O(10^{-2})$$

which is sufficiently small to assume that rapid distortion can be a viable mechanism even in our case (Jayaram *et al.* 1989). Secondly, there can be a 'pumping' effect due to 'shock-flapping' or LSSM (see § 10.2.4 of Smits & Dussauge 1996). Aside from the uncertain comparison between experiment and DNS, we achieve similar amplification rates of turbulent fluctuations to those observed by Smits & Muck (1987) and a 'pumping' mechanism is not relevant since there is no LSSM in our DNS.

REFERENCES

ACKERET, J., FELDMANN, F. & ROTT, N. 1946 Untersuchungen an Verdichtungsstößen und Grenzschichten in schnell bewegten Gasen. *Tech. Rep.* Mitt. Inst. Aerodyn. 10. ETH Zürich, Zürich, Switzerland.

ADAMS, N. A. 1997 DNS of shock boundary-layer interaction – preliminary results for compression ramp flow. In *CTR Annual Research Briefs 1997*. Center for Turbulence Research, Stanford University and NASA Ames Research Center, Stanford, California.

ADAMS, N. A. 1998 Direct numerical simulation of turbulent compression corner flow. *Theoret. Comput. Fluid Dyn.* **12**, 109–129.

ADAMS, N. A. & SHARIFF, K. 1996 A high-resolution hybrid compact-ENO scheme for shock–turbulence interaction problems. *J. Comput. Phys.* **127**, 27–51.

ADAMSON, T. C. & MESSITER, A. F. 1980 Analysis of two-dimensional interactions between shock waves and boundary layers. *Ann. Rev. Fluid Mech.* **12**, 103–138.

ANDREOPOULOS, J. & MUCK, K. C. 1987 Some new aspects of the shock-wave/boundary-layer interaction in compression-ramp flows. *J. Fluid Mech.* **180**, 405–428.

ARDONCEAU, P., LEE, D. H., ALIZARY DE ROQUEFORT, T. & GOETHALS, R. 1979 Turbulence behaviour in a shock wave/boundary layer interaction. In *AGARD CP*-271, pp. 8–1–8–14. AGARD Neuilly Sur Seine, France.

BLACKWELDER, R. F. & HARITONIDIS, J. H. 1983 Scaling of the bursting frequency in turbulent boundary layers. *J. Fluid Mech.* **132**, 87–103.

BLAISDELL, G. A., MANSOUR, N. N. & REYNOLDS, W. C. 1993 Compressibility effects on the growth and structure of homogeneous turbulent shear flow. *J. Fluid Mech.* **256**, 443–485.

BRANKOVIC, A. & ZEMAN, O. 1994 Effects of turbulence compressibility and unsteadiness in compression corner flow. In *CTR Proc. 1994 Summer Program*, pp. 301–311. Stanford, California, Center for Turbulence Research, Stanford University and NASA Ames Research Center.

DEBIÉVE, J.-F., DUPONT, P., SMITH, D. R. & SMITS, A. J. 1997 Supersonic turbulent boundary layer subjected to step changes in wall temperature. *AIAA J.* **35**, 51–57.

DOLLING, D. S. 1998 High-speed turbulent separated flows: consistency of mathematical models and flow physics. *AIAA J.* **36**, 725–732.

DOLLING, D. S. & MURPHY, M. T. 1983 Unsteadiness of the separation shock wave structure in a supersonic compression ramp flowfield. *AIAA J.* **12**, 1628–1634.

DOLLING, D. S. & OR, C. T. 1985 Unsteadiness of the shock wave structure in attached and separated compression ramp flows. *Exps. Fluids* **3**, 24–32.

ERENGIL, M. E. & DOLLING, D. S. 1991a Unsteady wave structure near separation in a Mach 5 compression ramp interaction. *AIAA J.* **29**, 728–735.

ERENGIL, M. E. & DOLLING, D. S. 1991b Correlation of separation shock motion with pressure fluctuations in the incoming boundary layer. *AIAA J.* **29**, 1868–1877.

FERNHOLZ, H. H., FINLEY, P. J., DUSSAUGE, J. P. & SMITS, A. J. 1989 A survey of measurements and measuring techniques in rapidly distorted compressible turbulent boundary layers. *AGARDograph* 315. AGARD, Neuilly sur Seine, France.

GATSKI, T. B. 1997 Modeling compressibility effects on turbulence. In *New Tools in Turbulence Modeling* (ed. O. Métais & J. Ferziger), pp. 73–104. Springer.

GREEN, J. E. 1970 Interaction between shock waves and turbulent boundary layers. *Prog. Aerosp. Sci.* **11**, 235–340.

HANIFI, A., SCHMID, P. J. & HENNINGSON, D. S. 1996 Transient growth in compressible boundary layer flow. *Phys. Fluids* **8**, 826–837.

HANNAPPEL, R. & FRIEDRICH, R. 1995 Direct numerical simulation of a Mach 2 shock interacting with isotropic turbulence. *Appl. Sci. Res.* **54**, 501–505.

HUANG, P. G., COLEMAN, G. N. & BRADSHAW, P. 1995 Compressible turbulent channel flows: DNS results and modelling. *J. Fluid Mech.* **305**, 185–218.

JAYARAM, M., DONOVAN, J. F., DUSSAUGE, J.-P. & SMITS, A. J. 1989 Analysis of rapidly distorted supersonic boundary layers. *Phys. Fluids* A **1**, 1855–1864.

JIMENEZ, J. & MOIN, P. 1991 The minimal flow unit in near-wall turbulence. *J. Fluid Mech.* **225**, 213–240.

KATZER, E. 1989 On the lengthscales of laminar shock/boundary-layer interaction. *J. Fluid Mech.* **206**, 477–496.

KELLER, J. & MERZKIRCH, W. 1990 Interaction of a normal shock with a compressible turbulent flow. *Exps. Fluids* **8**, 241–248.

LAUNDER, B. E., REECE, G. J. & RODI, W. 1975 Progress in the development of a Reynolds stress turbulence closure. *J. Fluid Mech.* **68**, 537–566.

LEE, S., LELE, S. K. & MOIN, P. 1993 Direct numerical simulation of isotropic turbulence interacting with a weak shock wave. *J. Fluid Mech.* **251**, 533–562.

LEE, S., LELE, S. K. & MOIN, P. 1997 Interaction of isotropic turbulence with shock waves: effect of shock strength. *J. Fluid Mech.* **340**, 225–247.

LELE, S. K. 1992a Compact finite difference schemes with spectral-like resolution. *J. Comput. Phys.* **103**, 16–42.

Lele, S. K. 1992*b* Shock-jump relations in a turbulent flow. *Phys. Fluids* A **4**, 2900–2905.

Lele, S. K. 1994 Compressibility effects on turbulence. *Ann. Rev. Fluid Mech.* **26**, 211–254.

Liepmann, H. W. 1946 The interaction between boundary layer and shock waves in transonic flow. *J. Aeronaut. Sci.* **13**, 623–637.

Maeder, T. 2000 Numerical investigation of supersonic turbulent boundary layers. PhD thesis, Diss. ETH No. 13662, ETH Zürich, Institute of Fluid Dynamics, Zürich, Switzerland.

Maeder, T., Adams, N. A. & Kleiser, L. 2000 Direct simulation of turbulent supersonic boundary layers by an extended temporal approach. To appear.

Mahesh, K., Lee, S., Lele, S. K. & Moin, P. 1995 The interaction of an isotropic field of acoustic waves with a shock wave. *J. Fluid Mech.* **300**, 383–407.

Mahesh, K., Lele, S. K. & Moin, P. 1993 Shock turbulence interaction in the presence of mean shear: an application of rapid distortion theory. *AIAA Paper* 93-0663.

Mahesh, K., Lele, S. K. & Moin, P. 1997 The influence of entropy fluctuations on the interaction of turbulence with a shock wave. *J. Fluid Mech.* **334**, 334–379.

Mahesh, K., Moin, P. & Lele, S. K. 1996 The interaction of a shock wave with a turbulent shear flow. *Tech. Rep.* TF-69. Department of Mechanical Engineering, Stanford University, Stanford, California.

Marshall, T. A. & Dolling, D. S. 1992 Computation of turbulent, separated, unswept compression ramp interactions. *AIAA J.* **30**, 2056–2065.

Moin, P. & Mahesh, K. 1998 Direct numerical simulation: a tool in turbulence research. *Ann. Rev. Fluid Mech.* **30**, 539–578.

Moser, R. D., Rogers, M. M. & Ewing, D. W. 1998 Self-similarity of time-evolving plane wakes. *J. Fluid Mech.* **367**, 255–289.

Na, Y. & Moin, P. 1996 Direct numerical simulation of turbulent boundary layers with adverse pressure gradient and separation. *Tech. Rep.* TF-68. Department of Mechanical Engineering, Stanford University, Stanford, California.

Na, Y. & Moin, P. 1998 Direct numerical simulation of separated turbulent boundary layer. *J. Fluid Mech.* **370**, 175–201.

Plotkin, K. J. 1975 Shock wave oscillations driven by turbulent boundary layer fluctuations. *AIAA J.* **13**, 1036–1040.

Ristorcelli, J. R. 1997 A pseudo-sound constitutive relationship for the dilatational covariances in compressible turbulence. *J. Fluid Mech.* **347**, 37–70.

Settles, G. S. & Dodson, L. J. 1991 Hypersonic shock/boundary-layer interaction database. *Tech. Rep.* NASA CR 177577. NASA Ames Research Center, Moffet Field, California.

Settles, G. S., Fitzpatrick, T. J. & Bogdonoff, S. M. 1979 Detailed study of attached and separated compression corner flowfields in high Reynolds number supersonic flow. *AIAA J.* **17**, 579–585.

Shu, C.-W. & Osher, S. 1989 Efficient implementation of essentially non-oscillatory shock-capturing schemes, II. *J. Comput. Phys.* **83**, 32–78.

Smits, A. J. & Dussauge, J.-P. 1996 *Turbulent Shear Layers in Supersonic Flow*. AIP Press, Woodbury, New York.

Smits, A. J. & Muck, K.-C. 1987 Experimental study of three shock wave/turbulent boundary layer interactions. *J. Fluid Mech.* **182**, 291–314.

Spina, E. F., Smits, A. J. & Robinson, S. K. 1994 The physics of supersonic turbulent boundary layers. *Ann. Rev. Fluid Mech.* **26**, 287–319.

Thomas, F. O., Putnam, C. M. & Chu, H. C. 1994 On the mechanism of unsteady shock oscillation in the shock wave/turbulent boundary layer interactions. *Exps. Fluids* **18**, 69–81.

Wilcox, D. C. 1989 Supersonic compression-corner applications of a multiscale model for turbulent flows. *AIAA J.* **28**, 1194–1198.

Wilcox, D. C. 1994 *Turbulence Modeling for CFD*. DCW Industries, La Cañada, California.

Williamson, J. H. 1980 Low-storage Runge–Kutta schemes. *J. Comput. Phys.* **35**, 48–56.